Manuscript File Click here to view linked References

On the Cycling of ^{231}Pa and ^{230}Th in Benthic Nepheloid Layers

Si-Yuan Sean Chen *

MIT-WHOI Joint Program in Oceanography, Massachusetts Institute of Technology, Cambridge, MA 02139, USA

Woods Hole Oceanographic Institution, Woods Hole, MA 02543, USA

Olivier Marchal

Woods Hole Oceanographic Institution, Woods Hole, MA 02543, USA

Paul E. Lerner

NASA Goddard Institute for Space Studies, New York City, NY 10026, USA

Daniel C. McCorkle

Woods Hole Oceanographic Institution, Woods Hole, MA 02543, USA

Michiel M. Rutgers van der Loeff

Alfred Wegener Institute for Polar and Marine Research, Bremerhaven, 27570, Germany

August 26, 2021

For Re-submission to Deep-Sea Research Part I: Oceanographic Research Papers

* *Corresponding author address:* Department of Earth, Atmospheric and Planetary Sciences, Massachusetts Institute of Technology, 77 Massachusetts Avenue, Cambridge, MA 02139, USA.

E-mail: osean@mit.edu

ABSTRACT

The naturally-occurring radionuclides protactinium-231 (^{231}Pa) and thorium-230 (^{230}Th) are produced at approximately uniform rates in the ocean and thought to be removed from the water column through a reversible exchange with settling particles. Recent measurements along the U.S. GEOTRACES North Atlantic transect (GA03) revealed two features which are at odds with current understanding about ^{231}Pa and ^{230}Th cycling in the ocean: (i) a sharp decrease in dissolved ^{231}Pa (^{231}Pa$_d$) and ^{230}Th (^{230}Th$_d$) activities with depth below 2000-4000 m and (ii) very high particulate ^{231}Pa (^{231}Pa$_p$) and ^{230}Th (^{230}Th$_p$) activities near the bottom, at a number of stations between the New England continental shelf and Bermuda. Concomitant measurements of light attenuation from beam transmissometry showed that both features occur in benthic nepheloid layers (BNLs), which suggests that these features may stem, at least partly, from the presence of resuspended sediment in the deep water column.

Here we explore the behaviour of ^{231}Pa and ^{230}Th in BNLs by using (i) radionuclide, optical, and hydrographic data from the western segment of GA03 (west of Bermuda) and (ii) a simplified model of particle and radionuclide cycling that includes a lateral particle source. First, the BNLs observed at GA03 stations are characterized from measurements of the beam attenuation coefficient converted to particle concentrations. At all stations, particle concentrations below the clear water minimum were the highest in the bottom mixed layer, whose thickness ranged from 95 to 320 m, and decreased generally with height above the bottom. The thickness of strong BNLs varied from 482 to 1358 m and the vertical integral of particle concentration in excess to that at the clear water minimum varied from 1×10^4 to 2×10^6 mg m^{-2}, among different stations. Second, the particle-radionuclide model is fitted to data from stations GT11-04 (New England continental rise) and GT11-08 (Hatteras abyssal plain), where samples for radionuclide analyses were collected in the BNL. The model can reproduce simultaneously the increase of particle concentration with depth, the low ^{231}Pa$_d$ and ^{230}Th$_d$ in the BNLs, and the high ^{231}Pa$_p$ and ^{230}Th$_p$ near the bottom. According to the model, at heights less than about 300 m above the seafloor, the dissolved phase was set primarily by a balance between adsorption and desorption, with vertical turbulent mixing playing a secondary role, whilst the particulate phase behaved largely as a non-reactive constituent supplied laterally and transported vertically by particle settling and turbulent mixing. Sensitivity tests with the model suggest that lateral particle sources near continental slopes and similar reliefs can produce significant biases both in the ^{230}Th normalization method and in the interpretation of sediment ^{231}Pa/^{230}Th records. Our findings yield insights into the influence of sediment resuspension and transport on ^{231}Pa and ^{230}Th in the deep ocean and highlight the need for considering these processes in paleoceanographic applications.

Keywords: nepheloid layer, thorium, protactinium, scavenging, sediment redistribution, GEOTRACES

1. Introduction

Protactinium-231 (half-life of 75.6 kyr; Cheng et al. (2013)) and thorium-230 (32.6 kyr; Jerome et al. (2020)) are two naturally-occurring radionuclides produced by the radioactive decay of ^{235}U and ^{234}U, respectively. As U isotopes appear to behave quasi-conservatively in seawater (e.g., Owens et al. (2011)), the production rates of ^{231}Pa and ^{230}Th are expected to be approximately uniform throughout the world's oceans, amounting to $2.33\times\ 10^{-3}$ dpm m^{-3} yr^{-1} and $2.52\times\ 10^{-2}$ dpm m^{-3} yr^{-1}, respectively (Yu et al. 1996). As a result, the ^{231}Pa/^{230}Th production ratio in the water column would also be approximately uniform and equal to 0.093.

In comparison to their sources, the sinks of ^{231}Pa and ^{230}Th in the ocean are poorly understood. Both radionuclides are thought to be removed from the water column through a reversible exchange with settling particles (e.g., Nozaki et al. (1981); Bacon and Anderson (1982)). In general, the distribution coefficient for ^{230}Th is greater than for ^{231}Pa (e.g., Moran et al. (2002), Hayes et al. (2015b)), which suggests that ^{230}Th is more particle-reactive than ^{231}Pa and that ^{231}Pa is generally more strongly influenced by ocean circulation than ^{230}Th. These characteristics prompted different applications of both radionuclides in chemical oceanography and paleoceanography. For example, the high affinity of Th for particles led to the use of ^{230}Th activity in sediment to correct accumulation rates for sediment lateral redistribution (Bacon 1984), and the disparate affinities of Pa and Th for particles led to the use of the sediment ^{231}Pa/^{230}Th activity ratio as an indicator of surface biological productivity (e.g., Kumar et al. (1995)) and meridional overturning circulation (Yu et al. 1996).

The distributions of ^{231}Pa and ^{230}Th in the North Atlantic have been documented in a number of studies. Data syntheses by Marchal et al. (2007) and Luo et al. (2010) illustrated that the activities of dissolved ^{231}Pa (^{231}Pa$_d$) and ^{230}Th (^{230}Th$_d$) across distant locations show (i) a similar increase with depth in the upper 1000 m but (ii) large lateral variations in the deeper water column. The abundant data sets collected along the U.S. GEOTRACES North Atlantic transect (GA03) have confirmed both features (i)-(ii) (Hayes et al. (2015a); their Fig. 2a). At deep stations along the western segment of GA03, between Woods Hole and Bermuda (line W), ^{231}Pa$_d$ and ^{230}Th$_d$ increased with depth to about 2000–4000 m, but decreased with depth below (Hayes et al. 2015a). Whereas the ^{231}Pa$_d$ and ^{230}Th$_d$ increase in the upper water column can be explained by exchanges with settling particles (Nozaki et al. 1981; Bacon and Anderson 1982), the processes responsible for the reversal in the vertical activity gradients near 2000–4000 m remain unclear. Equally unclear are the factors causing the extremely high activities of particulate ^{231}Pa (^{231}Pa$_p$) and ^{230}Th (^{230}Th$_p$) in near-bottom samples collected at a number of stations along line W (Hayes et al. 2015a), although the proximity of these samples to the seafloor points to an influence from sediment resuspension.

Interestingly, the ^{231}Pa and ^{230}Th activity anomalies observed in deep waters in the western North Atlantic occur in benthic nepheloid layers (Hayes et al. 2015a; Lerner et al. 2020). Benthic nepheloid layers (BNLs) are particle-rich layers that can be present in the lower part of the water column. They can extend vertically over a thousand meters or more and are thought to be produced by sediment resuspension followed by some combination of vertical mixing and lateral transport (McCave 1986; Gardner et al. 2018a). They can often be subdivided into two sublayers: (i) a lower sublayer in contact with the seabed where particle concentrations are the highest and which roughly coincides with the bottom mixed layer (BML) as identified by uniform potential temperature, and (ii) an upper sublayer in which particle concentration decreases upwards up to a clear water minimum. The thickness of the lower sublayer is $\mathcal{O}$(10 m) to $\mathcal{O}$(100 m) (of the order of 10–100 m), whereas the thickness of the upper sublayer can be $\mathcal{O}$(1000 m).

Strong BNLs, with particle concentrations consistently > 20 mg m^{-3} (Gardner et al. 2018b), have long been recognized from light scattering data as common features in the western North Atlantic below the depth of 3000 m, where a clear water minimum is typically found (Eittreim et al. 1969; Biscaye and Eittreim 1977). More recently, Lam et al. (2015) reported large variations of particle concentrations in deep waters along the western segment of GA03, with maxima up to $\mathcal{O}$(1000 mg m^{-3}) in BNLs, higher than in surrounding waters by two orders of magnitude. From an extensive compilation of nephelometer and transmissometer data, Gardner et al. (2017) estimated that the depth-integrated particle concentration in excess to that expected from the clear water minimum decreases eastward by up to one order of magnitude in the western North Atlantic (their Fig. 1). Such observations suggest that enhanced particle scavenging in BNLs might explain the low dissolved ^{231}Pa and ^{230}Th activities measured at abyssal depths in this region (e.g., Hayes et al. (2015a)). Similarly, sediment resuspension might also account for the very high particulate ^{231}Pa and ^{230}Th activities (expressed in dpm per volume of water) observed near the bottom at a number of GA03 stations (Hayes et al. 2015a).

Recently, Lerner et al. (2020) used a regional circulation model including ^{231}Pa and ^{230}Th to explore the potential of two processes to produce the relatively low ^{231}Pa$_d$ and ^{230}Th$_d$ observed at abyssal depths in the western North Atlantic: (i) the enhanced scavenging in BNLs, and (ii) the ventilation of western basins by ^{231}Pa- and ^{230}Th-poor waters from the Deep Western Boundary Current (DWBC). In their model, particle scavenging was constrained from a distribution of particulate matter concentration derived from optical measurements compiled by Gardner et al. (2017). They found that increased removal of both nuclides from solution in BNLs is more likely than ventilation by the DWBC to produce the small ^{231}Pa$_d$ and ^{230}Th$_d$ observed at depth. Interestingly, they also indicated that none of their model experiments could explain simultaneously the low dissolved activities and high particulate activities observed in deep waters at several GA03 stations along line W.

The effects of particle resuspension on Pa and Th isotope activities in near-bottom waters and surface sediment have been investigated in a few studies. Water samples from BNLs in the western North Atlantic (e.g., Bacon and Rutgers van der Loeff (1989)) and eastern North Atlantic (e.g., Turnewitsch and Springer (2001); Peine et al. (2009)) showed significant depletion of ^{234}Th (half-life of 24.1 d) relative to its radioactive parent (^{238}U), presumably as a result of intensified scavenging near the bottom. Bacon and Rutgers van der Loeff (1989) concluded that their observations from the western North Atlantic are best explained by local or nearby sediment entrainment from the seabed. Radioactive disequilibria were also observed in the BNL on the western slope of the Yermak Plateau, northwest of the Spitzbergen (Rutgers van der Loeff et al. 2002). The ^{234}Th depletion was found to be balanced by a similar excess in surface sediment, which was interpreted as implying the existence of a settling-resuspension loop with an average particle residence time of 1-2 months. Likewise, activity ratios $^{234}\mathrm{Th}/^{238}\mathrm{U} < 1$ in water samples collected near the seafloor in the eastern North Atlantic were interpreted as reflecting fast ^{234}Th scavenging due to active sediment resuspension (Peine et al. 2009). In sediment samples from the eastern South Atlantic and the Atlantic sector of the Southern Ocean, Kretschmer et al. (2010) noticed that ^{230}Th activity varies strongly with grain size, with 50–90% of total ^{230}Th inventory concentrated in material smaller than 10 μm, suggesting a particle sorting effect during sediment redistribution. More recently, the sensitivity of the $^{231}\mathrm{Pa}/^{230}\mathrm{Th}$ ratio of bulk sediment to sediment composition and redistribution has been investigated from two neighbouring sediment cores with distinct accumulation rates in the Atlantic sector of the Southern Ocean (Kretschmer et al. 2011). These authors found that the bulk $^{231}\mathrm{Pa}/^{230}\mathrm{Th}$ is not significantly influenced by sediment focusing (selective deposition of sediment), although their calculations suggested that particle sorting by selective removal of sediment (winnowing) could change the isotopic ratio. In the low and mid-latitude North Pacific (8–40°N), the observed depletion of total (dissolved + particulate) ^{230}Th in deep waters compared to values expected from reversible exchange was interpreted partly in terms of enhanced scavenging near the bottom (Okubo et al. 2012). These authors argued that large vertical mixing rates due to the complex topography of the western Pacific might transport the low ^{230}Th anomalies upward into the water column.

In this study, we aim to further our understanding of the apparent influence of BNLs on the distribution of ^{231}Pa and ^{230}Th in the western North Atlantic (Lerner et al. 2020). First, the hydrographic and turbidity conditions that prevailed at abyssal depths between the New England continental shelf and Bermuda during GA03 are characterized. A simplified model of particle and radionuclide cycling in the deep water column is then developed in which the BNL is created by a lateral particle source. The model is fitted to data from two GA03 stations in order to assess its ability to reproduce simultaneously the observed distributions of particle concentration and of radionuclide activities in both dissolved and particulate forms. The model is then applied to elucidate the influence of a lateral supply of particles on the ^{231}Pa and ^{230}Th activities of

particles settling to the seafloor.

The remainder of this paper is organized as follows. In section 2, the oceanographic data that are analysed in this study are briefly presented. The model of particle and radionuclide cycling is detailed in section 3. The hydrographic and turbidity conditions in deep waters along the western segment of GA03 are described and the particle-radionuclide model is fitted to data from two GA03 stations (GT11-04 and GT11-08) in section 4. In section 5, we propose a budget for ^{231}Pa and ^{230}Th in the lower part of the water column at GT11-04 and GT11-08, clarify the potential paleoceanographic implications of our results, outline model limitations, and suggest future directions of research. Finally, a summary follows in section 6.

2. Data

The oceanographic data used in this study originate from the second leg of the U.S. GEOTRACES North Atlantic transect (GA03), available from the second version of the Intermediate Data Product of GEOTRACES (Schlitzer et al. 2018). The second leg of GA03 was completed during cruise KN204-1 from Woods Hole, USA, to Praia, Cape Verde, via St. Georges, Bermuda, in November-December 2011 (**Fig. 1**). The stations occupied during this cruise are labelled as GT11-n, where n is the station number. We use *in situ* temperature, salinity, and pressure data from the CTD mounted on the GEOTRACES carousel "GTC" rosette (30-liter Niskin "ODF" rosette for station GT11-04) to characterize hydrographic conditions at GA03 stations along line W. Potential temperature is calculated from *in situ* temperature, salinity, and pressure using the algorithm of Jackett et al. (2006). Measurements of silicate concentration along GA03 are also used to further describe the hydrography at the occupied stations.

Measurements of ^{230}Th and ^{231}Pa activities in the dissolved and particulate fractions along GA03 were obtained on samples collected by, respectively, Niskin bottles and *in situ* filtration (Hayes et al. 2015a; Lam et al. 2015). Both size fractions are defined by the filtering procedures, with the "dissolved" fraction referring to the material with size < 0.45 μm and the particulate fraction referring to the material with size from 0.45 to 51 μm. The activity measurements were collaboratively produced by the Lamont-Doherty Earth Observatory, the Woods Hole Oceanographic Institution, and the University of Minnesota (Hayes et al. 2015a).

Light attenuation data from beam transmissometry are considered in this study in order to estimate the vertical distribution of particulate matter (PM) with high resolution in the lower water column at GA03 stations. Beam transmissometers were mounted on a GTC rosette and measured the beam attenuation coefficient for particles, c_p. In this paper, the c_p values are converted to PM concentrations, C, using the empirical relationship reported by Gardner et al. (1985b, 2018b) from data collected in the Nova Scotia rise

area during the High Energy Benthic Boundary Layer Experiment (HEBBLE),

$$C = 1208 \cdot c_p. \tag{1}$$

Here C is in mg m^{-3} and c_p is in m^{-1}. The relationship between C and c_p data obtained during HEBBLE was approximately linear up to $C = 2000$ mg m^{-3}, with a linear correlation coefficient of 0.97, beyond which data were insufficient or the attenuation signal returned by the transmissometer was saturated (Gardner et al. (1985b), their Fig. 4). The calibration (1) was established from data collected in intense BNLs with a maximum total suspended particulate matter concentration up to 12,700 mg m^{-3} (Gardner et al. 1985b).

The relationship between C and c_p is not universal, as it is expected to vary with particle properties such as size distribution and refraction index (e.g. Boss et al. (2018); Gardner et al. (2018b)). Use of HEBBLE calibration for our study is justified as follows. To our knowledge, the HEBBLE area on the Nova Scotia rise is the closest area to our study region for which a calibration between C and c_p in the lower water column has been established; it is located in water depths of about 3000–5000 m and at about 500 km to the northeast of line W (**Fig. 1**). Core top observations of two transects along the base of the New England rise (Bulfinch and Ledbetter 1983) show sediment textures that are similar to those of the HEBBLE area, with silt and mud comprising the majority of surface sediment (Driscoll et al. 1985). Although C and c_p data from GA03 have been obtained at GA03 stations (Lam et al. 2015; Schlitzer et al. 2018), we have refrained from using these data to establish a calibration specific to GA03 stations, as the particle concentration data (Lam et al. 2015) are too scarce and show too large variability to determine with confidence the relationship between C and c_p for $C > 200$ mg m^{-3} (Appendix A).

Finally, the bathymetric data used in this study originate from the 2-minute resolution ocean depth data base from the Global Multi-Resolution Topography (**Fig. 1**; Ryan et al. (2009)). The water depth at GA03 stations is taken from the GTC rosette lowered at each station, with the exception of station GT11-04 for which the water depth as reported by the ODF rosette is used.

3. Model

In this section, we present a model that describes the cycling of particulate matter and radionuclides (^{230}Th and ^{231}Pa) in the deep water column above the seafloor. This model is one-dimensional in the sense that the transport processes that are explicitly represented – particle settling and vertical turbulent mixing – move material only in the vertical direction. The resupension of surficial sediment from nearby topographic elements (e.g., continental slope and seamounts) and its subsequent lateral transport (e.g., Armi (1978); McCave (1983)) are combined and included implicitly as an external source in the model.

The model domain is intended to represent the benthic nepheloid layer (**Fig. 2**), specifically the strong BNL where particle concentrations are consistently greater than 20 mg m^{-3} (Gardner et al. 2018b). It consists of two sublayers: a lower sublayer in contact with the seafloor and where vertical turbulent mixing is intense, and an upper sublayer where mixing is reduced. The lower sublayer is the BML, and the upper sublayer, termed the upper BNL, is the more stratified portion of the water column above the BML.

a. Particulate Matter

The particle component of the model considers the following processes: (i) settling due to gravity, (ii) vertical turbulent mixing, and (iii) a particle source that represents the resuspension and subsequent lateral transport of sediment. The governing equation for particulate matter is therefore

$$\frac{\partial C}{\partial t} + \frac{\partial}{\partial z}(w_p C) = \frac{\partial}{\partial z}\left(\kappa_z \frac{\partial C}{\partial z}\right) + j_C. \tag{2}$$

Here t is time, z is the height above the seafloor, w_p is the particle settling velocity, κ_z is the vertical eddy diffusivity, and j_C is the particle source. Equation (2) states that the mass of particles per unit water volume changes as a result of the divergence of the particle settling flux, the divergence of the turbulent mixing flux, and/or the supply of particles from sediment resuspension and lateral transport. These three processes are discussed in turn below.

Consider first particle settling. The mean and median sizes of particles in the BNLs of the Nova Scotia rise observed during HEBBLE have been determined to range approximately from 10 to 30 μm by wet sieving and Coulter Counter analyses (Gardner et al. (1985a), their Fig. 10). Assuming a particle diameter of 20 μm, a particle density of 1500 kg m^{-3} (Gardner et al. (1985a); their Fig. 7), a deep water density of 1050 kg m^{-3}, and a kinematic viscosity of 1.43×10^{-6} m^2 s^{-3} (McCave (1984); his Table 1) yields a Stokesian particle settling speed of 5.8 m d^{-1}, the value considered in our study. The same value of settling speed has been used in the model of Rutgers van der Loeff and Boudreau (1997) to study the exchange of particles and ^{234}Th between the seabed and the benthic boundary layer, defined as the layer above the seabed directly affected by the sediment-water interface (Boudreau and Jørgensen 2001).

Consider then turbulent mixing. In our model, the vertical eddy diffusivity κ_z is taken as uniform both in the BML (layer 1) and in the upper BNL (layer 2), with $\kappa_{z,1} > \kappa_{z,2}$ (**Fig. 2**). This representation of the deep water column as two layers with uniform but distinct κ_z in each layer is consistent with the observed vertical distribution of radon-222 (^{222}Rn, half-life of 3.8 d), a tracer emanating from the seafloor, at several locations in the Hatteras abyssal plain (Sarmiento and Biscaye 1986). For reference, these authors reported estimates of vertical eddy diffusivity of the order of 4×10^2 m^2 d^{-1} (5×10^{-3} m^2 s^{-1}) in the BML and of the order of 9 m^2 d^{-1} (1×10^{-4} m^2 s^{-1}) in the stratified layer above it, although the diffusivity estimates

for both layers varied considerably between different locations (Sarmiento and Biscaye (1986); their Table 2).

Finally, consider the particle source due to resuspension and transport (collectively, "redistribution") of sediment particles. In our model, the strength of the particle source is assumed to decrease exponentially with height above the seabed,

$$j_C = j_{C,0}\, e^{-z/\delta_r}, \tag{3}$$

where $j_{C,0}$ is the strength of the particle source at the seafloor and δ_r is a vertical scale. The formulation (3) represents the injection of sediment in the deep water column from non-local sediment resuspension and has appeared in the model of particle exchange between the seabed and the bottom boundary layer developed by Boudreau (1997) and extended by Rutgers van der Loeff and Boudreau (1997) to include ^{234}Th and other species. It is consistent with the expected upward decrease in the lateral supply of resuspended sediment to the deep water column along, or near, the continental slope and rise: particles entrained from the continental slope and rise are expected to settle as they are transported offshore, leading to a larger flux of material near the base of the water column than above. It should be stressed, however, that the formulation (3) is chosen for simplicity and that no observations seem to be presently available to support or refute it. Accordingly, it should be considered as a hypothesis. McCave (1983) (his Fig. 18) found that detached turbid layers along the Nova Scotia continental rise observed during HEBBLE were confined to the bottom 500 m of the water column, consistent with the preferential injection of resuspended sediment near the bottom. Boudreau (1997) showed that his model based on formulation (3) can closely reproduce particle concentration data collected in the bottom 10 m of the water column at a location on the Oregon Shelf (Boudreau (1997); his Fig. 13). Similarly, we explore below (section 4.b) whether our model based on this formulation can reproduce the vertical distribution of particle concentration observed in the deep water column at stations GT11-04 and GT11-08.

The formulation (3) includes two parameters: δ_r and $j_{c,o}$. The scale δ_r depends both on (i) the nature of the physical processes leading to the resuspension of particles from the seabed and (ii) the height above the local seafloor of surrounding topographic features. Different physical processes redistribute sediment over different scales along the water column. Saltation introduces sediment up to heights a few particle diameters from the seabed, turbulent bursting or vortex shedding off of seafloor irregularities may inject sediment to heights up to several centimetres, and large eddies of the scale of the benthic boundary layer may redistribute sediment through much of the layer (Hill and McCave 2001). The height scales considered by Boudreau (1997) range from $\delta_r = 0.1$ to 1 m. Hill and McCave (2001) reported solutions of the model of Boudreau (1997) that have been obtained with $\delta_r = 0.1$, 2, and 50 cm. The lowest value was used to study the effect of a modest increase in injection height relative to the conventional 2-coarse grain diameter

height, the middle value would represent "turbulent bursts or eddies shed from bedforms", and the largest value would mimic the effect of "large sediment puffs that are observed to erupt from the lower part of the benthic boundary layer" (Hill and McCave 2001). All the preceding values are considerably smaller than the vertical scale of the BNL and even of the BML, indicating that δ_r as defined in our study would be significantly larger.

The strength of particle source at the seafloor, $j_{C,0}$, is also difficult to estimate and likely variable, depending on factors such as the shear stress exerted on the seafloor by near-bottom currents (Mengual et al. 2017). Rough estimates of $j_{C,0}$, however, could be obtained from the following approach. The integral of $j_c(z)$ from the seafloor to a height $\gg \delta_r$ is approximately $j_{C,0}\delta_r$, showing that the particle source strength at the seafloor could be estimated by dividing the particle source integrated over the water column by the vertical scale δ_r. At steady state, the particle source integrated over the water column should be balanced by a particle flux of the same magnitude to the seafloor. Sediment traps were deployed at 10 m above the bottom (m.a.b.) between 4100 and 5100 m at each of six moorings in the HEBBLE area, a region characterized by strong near-bottom currents (Gardner et al. 1983). Particle fluxes were monitored with additional traps deployed at 23, 54, 100, 200, and 500 m.a.b. on the mooring at 4950 m. The authors found that the particle flux at 500 m.a.b. for the 2-week period, consisting mostly of primary particles from surface water, was 166 mg m^{-2} d^{-1} and increased exponentially towards the bottom. The particle flux at 10 m.a.b. was much larger, increasing down slope from 1160 mg m^{-2} d^{-1} at 4158 m to a maximum of 77,300 mg m^{-2} d^{-1} at 5022 m, and then decreasing to 59,400 mg m^{-2} d^{-1} at the mooring at 5076 m (Gardner et al. 1983). These observations suggest that the flux of resuspended particles at 10 m.a.b. largely exceeded the flux of primary particles and ranged from $\mathcal{O}(10^3$ mg m^{-2} $d^{-1})$ to $\mathcal{O}(10^5$ mg m^{-2} $d^{-1})$. These latter values would correspond to a particle source near the seafloor of, respectively, $\mathcal{O}(10$ mg m^{-3} $d^{-1})$ and $\mathcal{O}(10^3$ mg m^{-3} $d^{-1})$, for a vertical scale $\delta_r = 100$ m; both values would be ten times larger for $\delta_r = 10$ m. In a subsequent study, sediment traps were deployed to sample vertical particle fluxes both just above and within the BNL on the continental slope and rise near the Hudson Canyon (**Fig. 1**) (Gardner et al. 1985a). The resuspended component of the particle flux was reported to be 39 mg m^{-2} d^{-1} and 129 mg m^{-2} d^{-1} at 100 and 13 m.a.b., respectively, on the upper rise, and 213 mg m^{-2} d^{-1} at 118 m.a.b. on the middle rise (Gardner et al. (1985a); their Table 1). Application of the same approach to the flux measured at 13 m.a.b. yields an estimate of the particle source near the seafloor of 1.29 (12.9) mg m^{-3} d^{-1} for $\delta_r = 100$ m ($\delta_r = 10$ m).

b. Radionuclides

The radionuclide component of our model represents the activities of ^{230}Th and ^{231}Pa in dissolved form (C_d) and in particulate form (C_p) separately (**Fig. 2**). The radionuclide activities as calculated by the model are intended to correspond to the activities measured on water samples and defined operationally by filtration (Hayes et al. 2015a). The governing equations for ^{231}Pa and ^{230}Th are based on the reversible exchange model (Nozaki et al. 1981; Bacon and Anderson 1982) with the added effects of vertical turbulent mixing and of an external particle source:

$$\frac{\partial C_d}{\partial t} = \frac{\partial}{\partial z}\left(\kappa_z \frac{\partial C_d}{\partial z}\right) + \beta + k_{-1}C_p - k_1 C_d, \tag{4a}$$

$$\frac{\partial C_p}{\partial t} + \frac{\partial}{\partial z}\left(w_p C_p\right) = \frac{\partial}{\partial z}\left(\kappa_z \frac{\partial C_p}{\partial z}\right) - k_{-1}C_p + k_1 C_d + B_r j_C. \tag{4b}$$

Here β is the rate of production from the radioactive parent (^{234}U for ^{230}Th and ^{235}U for ^{231}Pa), k_1 (k_{-1}) is an apparent first-order rate constant for Th or Pa adsorption onto (desorption from) particles, and B_r is the radionuclide activity per mass of resuspended particles. Equation (4a) states that the amount of radionuclide dissolved in a given volume of water changes as a result of the divergence of the turbulent mixing flux, the radioactive production, and/or the net transfer from the particulate phase from sorption reactions. Similarly, equation (4b) states that the amount of radionuclide bound to particles in a given volume of water varies due to the divergence of the particle settling flux, the divergence of the turbulent mixing flux, the net transfer from the dissolved phase, and/or a particle source. Radioactive decay is omitted from (4a)-(4b) since for the long-lived radioisotopes ^{230}Th and ^{231}Pa it is negligible compared to the exchanges between the solid and dissolved phases (e.g., Nyffeler et al. (1984); Geibert and Usbeck (2004); Lerner et al. (2017)). Implicit in the model is that the radionuclides bound to the source particles are able to exchange with the dissolved phase, with a variable intensity depending on the magnitude of the rate constants, namely k_1 and k_{-1}.

Theoretical considerations on sorption reactions in natural waters (Honeyman et al. 1988; Honeyman and Santschi 1989) and analysis of GA03 data (Lerner et al. 2017) suggest that the apparent first-order rate constant for metal adsorption onto particles increases with the concentration of particles. In our model, the adsorption rate constants for Th and Pa are assumed to be proportional to particle concentration, i.e.,

$$k_1 = k_{1,c} C, \tag{5}$$

where $k_{1,c}$ is a parameter that describes the sensitivity of the adsorption rate constant to the concentration of particulate matter. For example, the value of $k_{1,c}$ for ^{230}Th has been estimated to $0.029 \pm 3.54 \times 10^{-4}$ m^3 mg^{-1} yr^{-1} (mean $\pm$ 1 standard deviation or STD) from an analysis of Th isotope data for deep waters at GA03 stations east of Bermuda (Lerner et al. 2017). Notice that the formulation (5) should also be

regarded as a hypothesis, although it is consistent with previous work (Honeyman et al. 1988; Honeyman and Santschi 1989; Lerner et al. 2017). Based on data of reported by Honeyman et al. (1988), Jeandel et al. (2015) argued that particle concentration may not significantly affect the solid-solution partitioning of Th in BNLs, although many processes may obscure the relationship between the solid-solution partitioning and the adsorption rate of metals in sea waters (e.g., Lerner et al. (2017)).

In summary, our model of particle and radionuclide cycling in the BNL is represented by the system of partial differential equations (2), (4a), and (4b). In this study, the tendency terms $\partial C/\partial t$, $\partial C_d/\partial t$, and $\partial C_p/\partial t$ are omitted from the governing equations, i.e., steady state is assumed. Indeed, we feel that the influence of sediment redistribution on ^{231}Pa and ^{230}Th should first be examined under the steady state assumption before transient effects be considered. Notice that the net effect of an external particle source on the radionuclide activities in either dissolved or particulate phase cannot easily be anticipated. For example, a particle source would enhance the adsorption rate of ^{230}Th and ^{231}Pa onto particles (via the dependency of k_1 on C), which would tend to decrease dissolved activities. On the other hand, since a particle source is accompanied by a source of radionuclides in the particulate phase ($B_r j_C$), it would enhance the particulate activities and hence the desorption rate of ^{230}Th and ^{231}Pa from particles, which would tend to increase dissolved activities. Which of these competing effects will dominate at steady state is unclear and is a question addressed in this work.

c. Boundary Conditions

Under the steady-state assumption, the governing equations for particles and radionuclides reduce to a system of ordinary differential equations of second order, with the vertical coordinate z as the independent variable. Accordingly, the solution of these equations requires two boundary conditions, here specified at the top of the upper BNL ($z = H$) and at the seafloor ($z = 0$). Below, we present the conditions that are assumed at these two locations for the particulate matter equation and for the radionuclide equations.

1) Particulate Matter

At the top of the BNL ($z = H$), the particle concentration is imposed,

$$[C]_H = C_H. \tag{6}$$

In this study, C_H, is fixed to 20 mg m^{-3}, consistent with the definition of a strong benthic nepheloid layer (Gardner et al. 2018b). Condition (6) assumes implicitly that particle concentration at the top of the BNL is not determined by processes that take place within the BNL but by other processes, such as particle

production in the surface water.

At the seafloor ($z = 0$), the diffusive flux of particles is assumed to vanish,

$$\left[\kappa_{z,1}\frac{\mathrm{d}C}{\mathrm{d}z}\right]_0 = 0. \tag{7}$$

This condition implies that the exchange of particles at the sediment-water interface does not involve an influence from vertical turbulent diffusion. It is consistent with a vanishing value of vertical eddy diffusivity at the seafloor, as postulated in a number of models of the turbulence in the benthic boundary layer (Smith 1975; Lavelle et al. 1984; McLean 1985; Wiberg et al. 1994; Boudreau 2001). Note that this condition does not take the effect of local resuspension into account.

2) Radionuclides

As in the case of particle concentration, the radionuclide activities in the dissolved and particulate forms are imposed at the top of the BNL ($z = H$),

$$[C_d]_H = C_{d,H}, \tag{8a}$$

$$[C_p]_H = C_{p,H}. \tag{8b}$$

For this study, $C_{d,H}$ and $C_{p,H}$ are obtained by linear interpolation of measurements closest to the top of BNL at GA03 stations. Similar to equation (6), condition (8) assumes that the radionuclide activities at the top of the BNL are determined by processes outside the BNL.

At the seafloor ($z = 0$), the diffusive flux of dissolved and particulate radionuclide is set to zero, as with the particle concentration,

$$\left[\kappa_{z,1}\frac{\mathrm{d}C_d}{\mathrm{d}z}\right]_0 = 0, \tag{9a}$$

$$\left[\kappa_{z,1}\frac{\mathrm{d}C_p}{\mathrm{d}z}\right]_0 = 0. \tag{9b}$$

Conditions (9a)-(9b) imply that the vertical eddy diffusivity, the vertical gradient of C_d and C_p, or both of these quantities, vanish at the bottom, and that the effect of local resuspension is not considered.

d. Method of Solution

The differential equations (2), (4a), and (4b) with the tendency terms omitted are solved numerically using finite differences. The model domain is represented with a grid that extends from the seafloor at $z = 0$ to the top of the deep water column at $z = H$. The top of the deep water column varies among GA03 stations to accommodate the variable depths at which samples near the top of the BNL were taken for radiochemical

analyses. Details about the numerical method used to solve the steady state form of equations (2), (4a), and (4b) are provided in Appendix B.

4. Results

a. Characterization of the Deep Water Column

In this section, we present a brief analysis of measurements of potential temperature (θ), salinity (S), PM concentration (C) derived from beam transmissometry, and ^{230}Th and ^{231}Pa activities in dissolved and particulate forms, at GA03 stations occupied between Woods Hole and Bermuda. Emphasis is placed on the distribution of these properties along the deep water column, particularly in the benthic nepheloid layers.

1) Hydrography

We first consider the different water masses that were present along the western segment of GA03. Compilation of potential temperature and salinity data for stations GT11-03, 04, 06, 08, and 10 shows that waters deeper than 3000 m at these stations had an average θ of approximately 2.3°C and an average S of approximately 34.9 (**Fig. 3**). As a reference, the $\theta - S$ diagram also displays the values determined by Jenkins et al. (2015) for three components of North Atlantic Deep Water: Denmark Strait Overflow Water (DSOW), Iceland-Scotland Overflow Water (ISOW), and Classical Labrador Sea Water (CLSW). It is seen that waters deeper than 3000 m at GT11-03, 04, 06, 08, and 10 could be described as variable mixtures of DSOW, ISOW, and CLSW. However, measurements of silicate concentration at these stations show an average value of about 35 μmol kg^{-1} (Schlitzer et al. 2018), which exceeds by approximately a factor of 4 the silicate concentrations of DSOW, ISOW, and CLSW as reported by Jenkins et al. (2015). This observation suggests that the silicate-rich Antarctic Bottom Water (AABW) contributed at least a fraction of the colder and denser waters that were present at these stations. Overall, these results are qualitatively consistent with the water mass analysis of GA03 data (Jenkins et al. 2015).

The vertical profiles of θ and S show that the stratification varied along the deep water column at GA03 stations, with a bottom region presenting relatively small θ and S gradients overlaid by a region with larger gradients (**Fig. 4**). The quasi-uniform values of both θ and S observed near the bottom suggest the presence of a bottom mixed layer (BML) with a thickness of up to $\mathcal{O}$(100 m), consistent with previous observations in the western North Atlantic (e.g., Armi (1978)). To quantify the degree of uniformity at each station, we

use a mixed-layer quality index (QI) (Lorbacher et al. 2006; Huang et al. 2018):

$$QI = 1 - \frac{\sigma_{\mathrm{SL}}}{\sigma_{1.5\mathrm{SL}}}. \tag{10}$$

Here σ_{SL} is the standard deviation of θ within the selected layer, and $\sigma_{1.5\mathrm{SL}}$ is the standard deviation of θ over the depth interval extending from the seafloor to 1.5 times the selected layer thickness. A value of QI exceeding 0.8 would indicate that the selected layer is well-mixed, i.e., a well-developed mixed layer, whereas $QI < 0.5$ would indicate that a mixed layer is not present (Lorbacher et al. 2006).

We find that the quality index for GT11-01, 02, and 03 is smaller than 0.5, suggesting that a BML was absent at these relatively shallow stations. On the contrary, for the deeper stations GT11-04 to GT11-10, the quality index ranges from 0.73 to 0.90 (**Table 1**), suggesting a well-developed BML was generally present, with a thickness varying from 95-105 m (GT11-04, 06, 08) to 320 m (GT11-10). These values are comparable, or exceed, the 10°×10° averaged BML thickness of about 80 m in the western North Atlantic based on θ data from the World Ocean Circulation Experiment (Huang et al. (2019); their Fig. 1).

2) Turbidity

Vertical profiles of particle concentration estimated from beam transmissometry (Eq. 1) reveal that strong benthic nepheloid layers were present at all deep stations along line W (**Fig. 5a**). The concentration estimates in deep waters are consistent with values from less than 100 to 4,000 mg m^{-3} derived from bottom-tethered nephelometers deployed from several months to about a year in the western North Atlantic (Gardner et al. 2017). The particle concentration profiles show minima of approximately 14.5–18.7 mg m^{-3} at water depths of 2988 m, 3066 m, 3463 m, and 3244 m at stations GT11-04, 06, 08, and 10, respectively (**Table 1**). These results are in line with (i) PM levels estimated from major composition data along line W (Lam et al. (2015); their Fig. 3a) and (ii) the typical depth of the clear water minimum at around 3000 m in the western North Atlantic (Gardner et al. 2017).

We first estimate the thickness of the entire BNL at the deep stations along line W from the height of the absolute c_p minimum above the seafloor. According to this criterion, the thickness of the entire BNL amounts to 784, 1516, 1463, and 1323 m at stations GT11-04, 06, 08, and 10, respectively (**Table 1**). These values exceed the approximate values of 250 m (GT11-04), 300 m (GT11-08), and 1100 m (GT11-10) reported by Lam et al. (2015) (their Table 2); the differences likely reflect the different approaches to determine BNL thickness (values reported by Lam et al. (2015) were estimated visually from the bottom to the depth where light transmission appears to return to its background value; P. Lam, *pers. comm.*). These values also appear greater than the BNL thicknesses in the western North Atlantic as mapped by Gardner et al. (2018a) (their Fig. 2).

We then estimate the thickness of the strong BNL at the same stations from the thickness of the deep water column below the depth where PM concentration is consistently > 20 mg m^{-3} (Gardner et al. 2018b). With this definition, the thickness of the strong BNL amounts to 482, 1358, 730, and 1031 m at stations GT11-04, 06, 08, and 10, respectively (**Table 1**). Although these values still exceed the BNL thickness at GT11-04 and GT11-08 reported by Lam et al. (2015), our estimate for GT11-10 is close to theirs. These values are also more consistent with the BNL thicknesses mapped by Gardner et al. (2018a).

In order to assess the intensity of the BNL at each station, we calculate the excess PM load (e.g., Gardner et al. (2017)), which is the integral, over the thickness of the entire BNL, of particle concentration relatively to that at the clear water minimum,

$$\int_0^H (C - C_H)\, dz. \tag{11}$$

We find that the excess PM load varies from 1×10^4 mg m^{-2} (GT11-10) to 2×10^6 mg m^{-2} (GT11-04) (**Table 1**), consistent with, or higher than, values mapped by Gardner et al. (2017) (their Fig. 1). The highest PM load is found at station GT11-04, where the BML presents high PM levels but is relatively thin, whilst the lowest PM load is found at station GT11-10, where the BML presents lower PM levels but is thicker.

Interestingly, the vertical distribution of PM concentration shows features that could be associated with features in the vertical distributions of θ and S at a number of stations (**Fig. 4**). Maxima in PM concentration are found in the BML at stations GT11-04, 06, 08 and 10, which suggests that they may have been caused by the upward transport of resuspended material from the seafloor by vigorous mixing. Moreover, close inspection of θ and PM profiles at stations GT11-04, 08 and 10 reveals step-like structures in the θ profiles that coincide with similar structures in the PM profiles in the upper part of the BNL. Such coincidence is particularly pronounced at GT11-10, close to Bermuda. Coinciding small-scale irregularities in potential temperature and nephelometer profiles have been previously discovered in the Sohm abyssal plain and interpreted as bottom turbid layers detached from nearby topographic elements (e.g., Armi (1978); McCave (1983)).

3) ^{230}Th and ^{231}Pa Activities

Dissolved ^{230}Th and ^{231}Pa activities ($^{230}\mathrm{Th}_d$, $^{231}\mathrm{Pa}_d$) tend to increase with depth down to approximately 2000–4000 m at all stations along line W (**Fig. 5b**). However, at the deep stations (GT11-04, 06, 08, and 10), $^{230}\mathrm{Th}_d$ and $^{231}\mathrm{Pa}_d$ tend to decrease with depth below 2000–4000 m. Thus, the vertical gradients of $^{230}\mathrm{Th}_d$ and $^{231}\mathrm{Pa}_d$ change sign at mid-depth, as previously illustrated by Hayes et al. (2015a) and Lerner et al. (2020). Interestingly, the depth of the $^{230}\mathrm{Th}_d$ and $^{231}\mathrm{Pa}_d$ inversions appears to broadly coincide with

the clear water minimum, where particle concentration is the lowest (**Fig. 5a-b**). At deep stations, the particulate ^{230}Th and ^{231}Pa activities ($^{230}\mathrm{Th}_p$, $^{231}\mathrm{Pa}_p$) show high values near the bottom (**Fig. 5c**). Water samples collected near the seafloor at stations GT11-04 and GT11-08, where intense BNLs were observed (**Fig. 5a**), present extremely high activities of particulate ^{230}Th (up to 5.0 dpm m^{-3}) and particulate ^{231}Pa (up to 0.27 dpm m^{-3}). These values exceed, respectively, the $^{230}\mathrm{Th}_d$ and $^{231}\mathrm{Pa}_d$ activities measured at similar depths. They are one order of magnitude greater than typical $^{230}\mathrm{Th}_p$ and $^{231}\mathrm{Pa}_p$ near the bottom at other stations and two orders of magnitude greater than typical $^{230}\mathrm{Th}_p$ and $^{231}\mathrm{Pa}_p$ near the clear water minimum (**Fig. 5c**). The increases of $^{230}\mathrm{Th}_p$ (about 4.0 dpm m^{-3}) and $^{231}\mathrm{Pa}_p$ (about 0.25 dpm m^{-3}) from near the top of the BNL to near the seafloor exceeded largely the downward decreases of $^{230}\mathrm{Th}_d$ (about 0.45 dpm m^{-3}) and $^{231}\mathrm{Pa}_d$ (about 0.10 dpm m^{-3}) over a similar depth interval, implying that the total activity increased with depth in the BNL for both radionuclides.

The ^{230}Th and ^{231}Pa activity anomalies observed in deep waters at GA03 stations west of Bermuda are reminiscent of the ^{234}Th activity anomalies measured at these stations (Owens et al. 2015). At GT11-08, in the lower 1000 m of the water column, particulate ^{234}Th increased with depth and total ^{234}Th was near radioactive equilibrium, implying that dissolved ^{234}Th inferred as the difference between total and particulate activities decreased towards the bottom; in the lower 1000 m at GT11-04, particulate ^{234}Th also increased with depth but total ^{234}Th was not measured (Owens et al. 2015; their Fig. 16). These results indicate that, at least at station GT11-08, the particulate (dissolved) activity increased (decreased) with depth in the BNL for both ^{230}Th and ^{234}Th, but that the total activities behave differently between the two radioisotopes.

b. Test of the Particle-Radionuclide Model

In this section, we examine whether the particle concentrations and radionuclide activities observed in the deep water column at GA03 stations can be reproduced by the particle-radionuclide model described in section 3. Emphasis is placed on observations from stations GT11-04 and GT11-08, where water samples for radionuclide analyses have been collected in the BNL and close to the seafloor (Hayes et al. 2015a). As shown above (**Fig. 5b-c**), these samples exhibit particularly high anomalies of ^{230}Th and ^{231}Pa, both in dissolved and particulate phases. A question of preeminent interest is whether the radionuclide anomalies measured in these samples could be explained by the combined effect of sediment resuspension and lateral transport as crudely represented in our model.

To address this question, the equations of the particle-radionuclide model (Appendix B) are fitted to the particle concentration and radionuclide activity data at stations GT11-04 and GT11-08 using a non-linear least-squares method (Tarantola and Valette 1982). This method, referred to as the Algorithm of Total

Inversion (ATI), allows prior estimates of model parameters and their uncertainties to be considered when fitting the model to the data (**Table 2**). It has been applied in a number of studies to estimate rates of particle cycling and Th sorption from particle and Th isotope data in the water column (e.g., Murnane et al. (1994, 1996); Lerner et al. (2016, 2017)). Details about the ATI can be found in Appendix C.

1) Fit to Particle Concentration Data

First, the particle transport model (Eq. 2) is fitted to particle concentration data derived from measurements of the beam attenuation coefficient in the BNL at stations GT11-04 and GT11-08. The model is fitted to particle concentration data in the bottom 600 m of the water column at station GT11-04 and in the bottom 800 m of the water column at station GT11-08. For the fit to particle concentration data at both stations, particles are assumed to settle at a velocity of $w_p = -5.8$ m d^{-1} (section 3a) and particle concentration at the top of the BNL is set to $C_H = 20$ mg m^{-3} (section 3c). The model fit to the data is achieved by varying four parameters: the particle source at the seafloor ($j_{C,0}$), the vertical scale of the particle source (δ_r), and the vertical eddy diffusivities in the BML ($\kappa_{z,1}$) and the upper BNL ($\kappa_{z,2}$) (Appendix C).

We find that, for both stations, the particle concentration profile derived from the fit agrees closely with the observed profile (**Fig. 6**). The best fit to GT11-04 data is obtained from $j_{C,0} = 156.8 \pm 5.3$ mg m^{-3} d^{-1}, $\delta_r = 78.3 \pm 2.6$ m, $\kappa_{z,1} = 162.0 \pm 12.3$ m^2 d^{-1}, and $\kappa_{z,2} = 104.3 \pm 16.9$ m^2 d^{-1} (estimated value $\pm$ 1 STD); the best fit to GT11-08 data is obtained from $j_{C,0} = 57.9 \pm 7.8$ mg m^{-3} d^{-1}, $\delta_r = 50.5 \pm 6.4$ m, $\kappa_{z,1} = 186.1 \pm 41.9$ m^2 d^{-1}, and $\kappa_{z,2} = 35.4 \pm 19.2$ m^2 d^{-1}. The parameter estimates for both stations are within 1 or 2 STDs of the prior estimates (**Table 2**). Interestingly, both the particle source at the seafloor and the vertical scale of the particle source are inferred to be significantly larger at station GT11-04 (water depth 3772 m), on the continental rise, than at station GT11-08 (4926 m), in the abyssal plain. Similarly, the diffusivity in the upper BNL is estimated to be greater at GT11-04 than at GT11-08, whereas the estimate of diffusivity in the BML is comparable between the two stations. Overall, these results suggest that the particle transport model (Eq. 2) can provide a good description of the particle concentration profiles at both stations, except for a number of features such as local maxima and small-scale irregularities (**Fig. 6**).

2) Fit to Radionuclide Data

Second, the radionuclide model (Eqs. 4) is fitted to the few radionuclide data which are available in the BNL at heights less than 600 m.a.b. at station GT11-04 and less than 800 m.a.b. at station GT11-08. For each station, particles are assumed to settle at a velocity of $w_p = -5.8$ m d^{-1} and the values of $j_{C,0}$, δ_r, $\kappa_{z,1}$, and $\kappa_{z,2}$ are those estimated from the inversion of PM data at the corresponding station (section 4b.1).

For station GT11-04, the radionuclide activities at the top of the BNL are set to $C_{d,H} = 0.5$ dpm m^{-3} and $C_{p,H} = 0.05$ dpm m^{-3} for ^{230}Th, and to $C_{d,H} = 0.2$ dpm m^{-3} and $C_{p,H} = 0.002$ dpm m^{-3} for ^{231}Pa. For station GT11-08, $C_{d,H} = 0.5$ dpm m^{-3} and $C_{p,H} = 0.05$ dpm m^{-3} for ^{230}Th, and $C_{d,H} = 0.17$ dpm m^{-3} and $C_{p,H} = 0.002$ dpm m^{-3} for ^{231}Pa. The model fit to the radionuclide data is achieved by varying three parameters: the second-order rate constant for Th or Pa adsorption onto particles ($k_{1,c}$), the first-order rate constant of Th or Pa desorption from particles (k_{-1}), and the resuspended sediment activity (B_r) (Appendix C). The balance equations (4a)-(4b) are fitted separately for each radionuclide, so that estimates of $k_{1,c}$, k_{-1}, and B_r are obtained separately for ^{230}Th and ^{231}Pa.

Consider first the fit to radionuclide data for station GT11-04. For ^{230}Th, the best fit to dissolved and particulate activity data is achieved with $k_{1,c} = 0.0068 \pm 0.0013$ m^3 mg^{-1} yr^{-1}, $k_{-1} = 0.204 \pm 0.050$ yr^{-1}, and $B_r = 3.67 \pm 0.11$ dpm g^{-1} (**Fig. 7 left**). For ^{231}Pa, the best fit to dissolved and particulate activity data is achieved with $k_{1,c} = 0.0022 \pm 0.0003$ m^3 mg^{-1} yr^{-1}, $k_{-1} = 0.908 \pm 0.121$ yr^{-1}, and $B_r = 0.302 \pm 0.009$ dpm g^{-1} (**Fig. 8 left**). For both ^{230}Th and ^{231}Pa, the posterior estimates of the adsorption and desorption rate constants are smaller than, but within 1 or 2 STDs of, prior estimates, except for k_{-1} for ^{230}Th which is significantly smaller than its prior value (**Table 2**). The posterior estimates of sediment ^{230}Th and ^{231}Pa activity (B_r) are both greater than prior estimates based on measurements of excess ^{230}Th and ^{231}Pa of sediment core tops at water depths between 384 and 2736 m in the Mid-Atlantic Bight (MAB; **Fig. 1**) (Anderson et al. 1994). Excess ^{230}Th activities in sediment core tops and sediment traps from the MAB (water depths from $<$ 500 m to 2500–3000 m) exhibit an increase with water depth, with a gradient of about 1 dpm g^{-1} km^{-1} (Anderson et al. (1994); their Fig. 2). Extrapolation of core-top excess ^{230}Th to depths $>$ 3000 m using linear regression suggests that ^{230}Th of surficial sediment at the water depth of GT11-04 (3772 m) would amount to 4.2 dpm g^{-1}; the B_r value derived from the fit is smaller than the extrapolated value and consistent with the excess ^{230}Th measurement near 2750 m (**Fig. 9a**). For excess ^{231}Pa, extrapolation to depths $>$ 3000 m using linear regression suggests that ^{231}Pa of surficial sediment at the water depth of GT11-04 would amount to 0.25 dpm g^{-1} (**Fig. 9a**), still smaller than the B_r value derived from the fit.

Consider then the fit to radionuclide data from station GT11-08. For ^{230}Th, a good fit to dissolved and particulate activity data is found with $k_{1,c} = 0.0038 \pm 0.0005$ m^3 mg^{-1} yr^{-1}, $k_{-1} = 0.052 \pm 0.016$ yr^{-1}, and $B_r = 6.96 \pm 0.73$ dpm g^{-1} (**Fig. 7 right**). Again the posterior estimates of the adsorption and desorption rate constants are smaller than prior estimates; the posterior estimate of $k_{1,c}$ is within 2 STDs of its prior value, and the posterior estimate of k_{-1} differs from its prior value by $>$ 2 STDs (**Table 2**). Similar to GT11-04, the posterior estimate of the resuspended sediment activity, B_r, exceeds the ^{230}Th activities of surface sediment and sediment trap particles in the MAB (Anderson et al. 1994). Extrapolation of core-top excess ^{230}Th to depths $>$ 3000 m using linear regression suggests that ^{230}Th of surficial sediment at the

water depth of GT11-08 (4926 m) would amount to 5.5 dpm g^{-1} (**Fig. 9a**), within 2 STDs of the B_r value derived from the fit. For ^{231}Pa, the best fit to dissolved and particulate activity data is obtained with $k_{1,c} = 0.0021 \pm 0.0003$ m^3 mg^{-1} yr^{-1}, $k_{-1} = 0.692 \pm 0.115$ yr^{-1}, and $B_r = 0.250 \pm 0.026$ dpm g^{-1} (**Fig. 8 right**). The sorption rate constants are smaller (significantly so for k_{-1}) than their prior estimates (**Table 2**). As with ^{230}Th, the value of B_r deduced from the fit exceeds, but is within 2 STDs of, its prior value, yet it is smaller than the extrapolated value of 0.32 dpm g^{-1} based on linear regression (**Fig. 9a**).

In summary, we find that the particle-radionuclide model can simultaneously reproduce three key observations in the BNL at station GT11-04, on the continental rise: (i) the high particle concentrations, (ii) the low $^{230}Th_d$ and $^{231}Pa_d$ activities, and (iii) the high $^{230}Th_p$ and $^{231}Pa_p$ activities. The model can also reproduce reasonably well the measurements gathered at GT11-08, in the abyssal plain, although results for that station are less conclusive given the lack of dissolved activity data near the bottom. Although additional measurements of radionuclide activities are clearly desirable, the agreement of model results with the data suggests that an external source of resuspended sediment may have contributed to the ^{230}Th and ^{231}Pa anomalies observed in the deep water column at both stations.

5. Discussion

In the previous section, we showed that the particle-radionuclide model considered in this study can broadly reproduce (i) the high particle concentrations, (ii) the low $^{230}Th_d$ and $^{231}Pa_d$ activities, and (iii) the high $^{230}Th_p$ and $^{231}Pa_p$ activities, which have been observed in the BNL at stations GT11-04 and GT11-08 (no dissolved radionuclide data are available near the bottom at GT11-08, so that results are less conclusive for this station). These results contrast with the difficulty of ocean circulation models that incorporate ^{230}Th and ^{231}Pa to closely reproduce the observed deep water activities in the two phases simultaneously (Rempfer et al. 2017; Gu and Liu 2017; van Hulten et al. 2018; Lerner et al. 2020). Interestingly, none of these models include, at least explicitly, the effects of sediment resuspension and transport on particle scavenging. Rempfer et al. (2017) found that a better agreement with radionuclide measurements is obtained by adding in their model ^{230}Th and ^{231}Pa sinks at the seafloor and at continental boundaries. Similarly, Lerner et al. (2020) showed that a simulation characterized by a non-uniform k_1 constrained from PM observations generally better replicates ^{230}Th and ^{231}Pa data in both phases than a simulation characterized with uniform k_1. Altogether, these previous results and ours suggest that the redistribution of sediment particles may significantly affect the distributions of ^{230}Th and ^{231}Pa in the deep ocean.

Evidence for an influence from sediment redistribution can also be found in ^{234}Th data collected at GA03 stations west of Bermuda (Owens et al. 2015). To reveal the information contained in these data, we apply

the balance equations for the radionuclide activities in dissolved form (4a) and particulate form (4b) to ^{234}Th. To account for the short half-life of ^{234}Th, the radioactive decay terms $-\lambda C_d$ and $-\lambda C_p$ are added to the right-hand side of (4a) and (4b), respectively. Summing the resulting equations yields, for steady state,

$$\frac{d}{dz}\left(w_p C_p\right) = \frac{d}{dz}\left(\kappa_z \frac{dC_t}{dz}\right) + \beta - \lambda C_t + B_r j_c, \tag{12}$$

where $C_t = C_d + C_p$ is the total ^{234}Th activity. Measurements in the lower 1000 m of the water column at GT11-08 show that total ^{234}Th was close to ^{238}U activity as estimated from salinity (Owens et al. 2015; their Fig. 16), i.e., the difference $\beta - \lambda C_t$ is inferred to vanish there (total ^{234}Th activity was not measured near the bottom at GT11-04, so no similar inference could be made for that station). Considering this result in (12) and integrating the resulting equation from the seafloor ($z = 0$) to the top of the BNL ($z = H$) lead to,

$$[w_p C_p]_H - [w_p C_p]_0 = [\kappa_z \frac{dC_t}{dz}]_H - [\kappa_z \frac{dC_t}{dz}]_0 + \int_0^H B_r j_c dz. \tag{13}$$

Total ^{234}Th data at GT11-08 suggest that the vertical activity gradient dC_t/dz was negligible both at $z = H$ and at $z = 0$ (Owens et al. 2015; their Fig. 16), although additional data, particularly near the seafloor, would be needed to confirm this. Equation (13) would then reduce to

$$[w_p C_p]_H - [w_p C_p]_0 = \int_0^H B_r j_c dz. \tag{14}$$

This equation states that the difference between the settling fluxes of particulate ^{234}Th at the top of the BNL and at the seafloor should be balanced by the vertical integral of the lateral particle source. In contrast to total ^{234}Th, measurements of particulate ^{234}Th at GT11-08 (and also at GT11-04) show a dramatic increase with depth in the bottom 1000 m of the water column (Owens et al. 2015; their Fig. 16), akin to the increase of particulate ^{230}Th measured at these stations (Fig. 5). Assuming that w_p at $z = H$ and $z = 0$ are comparable, consideration of this other observation would imply that the left-hand side of (14), and hence the right-hand side of (14), are positive (since w_p is negative from our sign convention for the z coordinate). Thus, under the stated assumptions, the available ^{234}Th data would require the presence of a lateral source of ^{234}Th-bearing particles near the bottom at GT11-08 (and possibly also at GT11-04).

In the remainder of this section, we first attempt to interpret the estimated values of the sorption rate constants for ^{230}Th and ^{231}Pa at GT11-04 and GT11-08 (Table 3). Next, we propose a tentative budget for ^{230}Th and ^{231}Pa in the BNL at both stations. We then explore the potential implications of our results for the interpretation of ^{230}Th and ^{231}Pa measurements from deep-sea sediment cores. Finally, we clarify the limitations of our model and suggest lines of future research.

a. Kinetics of ^{230}Th and ^{231}Pa in the BNL

Our posterior estimates of the adsorption and desorption rate constants ($k_{1,c}$ and k_{-1}) for ^{230}Th and ^{231}Pa are smaller than their prior estimates for both GT11-04 and GT11-08. For ^{230}Th, our posterior estimates of $k_{1,c}$ are 0.0068 ± 0.0013 m^3 mg^{-1} yr^{-1} and 0.0038 ± 0.0005 m^3 mg^{-1} yr^{-1} for GT11-04 and GT11-08, respectively (Table 3). Both values are much smaller than the prior estimates of (i) 0.029 m^3 mg^{-1} yr^{-1} based on a previous analysis of GA03 data collected outside BNLs (Lerner et al. 2017) and (ii) 0.024 m^3 mg^{-1} yr^{-1} based on a compilation of laboratory and field data of Th isotopes (Honeyman et al. 1988). Similarly, our estimates of k_{-1} are 0.204 ± 0.050 yr^{-1} for GT11-04 and 0.052 ± 0.016 yr^{-1} for GT11-08 (Table 3), which are both smaller than our prior estimate of 1.0 yr^{-1} based on analyses of field data from outside BNLs (for a compilation, see Marchal and Lam (2012)). For ^{231}Pa, given the little knowledge of $k_{1,c}$ and k_{-1} compared to ^{230}Th, prior estimates of $k_{1,c} = 0.0029$ m^3 mg^{-1} yr^{-1} and $k_{-1} = 1$ yr^{-1} were assumed, where the low value of $k_{1,c}$ relatively to that for ^{230}Th is intended to reflect the generally lower affinity of Pa compared to Th for marine particles (e.g., Moran et al. 2002; Hayes et al. 2015b). Our least-square estimates of $k_{1,c}$ are 0.0022 ± 0.0003 m^3 mg^{-1} yr^{-1} for GT11-04 and 0.0021 ± 0.0003 m^3 mg^{-1} yr^{-1} for GT11-08 (Table 3), which are also smaller than their prior values. Similarly, our estimates of k_{-1} are 0.908 ± 0.121 yr^{-1} for GT11-04 and 0.692 ± 0.115 yr^{-1} for GT11-08 (Table 3), which are also smaller than their prior value.

The relatively small values of $k_{1,c}$ and k_{-1} estimated for ^{230}Th and ^{231}Pa in the BNL at stations GT11-04 and GT11-08, compared to prior values estimated for other oceanic environments, suggest that Th and Pa are less exchangeable with resuspended particles than with primary particles. The distinct exchangeability could result from differences in the chemical composition between resuspended and primary materials. Gardner et al. (1985a) noted that such differences in composition could be caused by (i) temporal variations in the composition of primary flux, (ii) diagenetic changes in the deposited sediment, (iii) differential resuspension of particles by type or size, or (iv) different original sources for the resuspended material and the primary material. Assuming a relatively long residence time of particulate material in surface sediments, we hypothesize that seafloor particles resuspended into the BNL could have acquired, at the sediment surface or within the sediment, coatings from adsorbed organic matter or by colonizing bacteria, or perhaps coatings of authigenic aluminosilicates, thereby modifying their sorptive properties.

Particles resuspended into the BNL, however, could be coated by materials that may enhance, not reduce, the adsorption rate of ^{230}Th and ^{231}Pa per unit particle concentration ($k_{1,c}$). During HEBBLE, Gardner et al. (1985a) reported (i) a diagenetic alteration of particles entrained from the seabed and (ii) the enrichment of Mn in the near-bottom suspended particles and surface sediments. Offshore transport

of ^{231}Pa by Mn-rich fine sediments was postulated to be responsible for the relatively low surface sediment ^{231}Pa/^{230}Th in the Mid-Atlantic Bight (Anderson et al. 1994). Consistent with the result of Gardner et al. (1985a), Lam et al. (2015) noted elevated concentrations of Mn (oxyhydr)oxide, calculated as excess Mn over crustal abundance, in small-sized particles (< 51 μm) collected in the BNL between GT11-03 and GT11-10. Iron and manganese coatings of particles have been postulated to enhance scavenging of ^{230}Th and ^{231}Pa at sites near hydrothermal vents in the North Atlantic (Hayes et al. 2015b) and the South Pacific (Pavia et al. 2018, 2019). Lerner et al. (2018) examined the influence of particle composition (biogenic particles, Mn (oxyhydr)oxides, Fe (oxyhydr)oxides, and lithogenic particles) on k_1 estimates for Th obtained from an inversion of Th isotope and particle concentration data from GA03 stations east of Bermuda. They found that the k_1 variance explained by particle composition is predominantly due to Mn (oxyhydr)oxides at stations west of the Mauritanian upwelling region, if the effect of the different particle types on scavenging is assumed to be multiplicative. In a recent review, Costa et al. (2020) pointed out that sediment grains could be coated by Fe-Mn oxides or other authigenic phases during diagenesis, which may enable the resuspended sediment to scavenge additional amounts of ^{230}Th from the water column and explain the observed decrease of dissolved ^{230}Th with depth (Hayes et al. 2015a). This process would yield elevated $k_{1,c}$ values, rather than smaller $k_{1,c}$ values as estimated here.

Speculatively, this apparent contradiction could be explained by the presence of organic coatings on resuspended particles, although evidence that organic coating of sediment grains would reduce their interaction with Th or Pa in seawater seems to be lacking. Albeit enriched in Fe and/or Mn, particles entrained from the seabed would exhibit a reduced ability to adsorb (and desorb) ^{230}Th and ^{231}Pa through the presence of organic material that would isolate the particle inner surface from solution, thereby explaining our relatively low $k_{1,c}$ (and k_{-1}) estimates. Another potential explanation is the saturation of the more reactive binding sites on particle surfaces by complexes other than Th complexes, though the reason for this saturation is unclear. Field observations have emphasized the role of specific organic compounds in the scavenging of Th and/or Pa isotopes in seawater (e.g., Roberts et al. (2009); Xu et al. (2011)). Our hypothesis, however, does not imply that the organic coating of sediment particles during diagenesis would prevent Th and Pa exchange with the dissolved phase as these particles are returned into the water column, but merely that such coating would reduce this exchange compared to that for primary particles. The ratio of the adsorption to desorption rate constants, k_1/k_{-1}, is generally better constrained by the data and better reflects the collective influence of particle scavenging, than k_1 and k_{-1} individually. In this light, the effect of diagenetic changes in particle composition may thus be two-fold: on one hand, the k_1/k_{-1} ratio may be increased by Mn oxide coatings, which would tend to enhance scavenging; on the other hand, organic coatings may reduce the overall exchange of particles with the surrounding seawater and thus reduce both $k_{1,c}$ and k_{-1}.

According to the model fit to data, the vertical profiles of k_1 for ^{230}Th and ^{231}Pa at GT11-04 and GT11-08 show a spectacular enhancement with depth in the BNL, up to approximately 15 yr^{-1} for ^{230}Th at GT11-04 (**Fig. 10**). It is worth noting that this value is comparable to the Th adsorption rate constant of 21 yr^{-1}, inferred at station GT11-16 near the Mid-Atlantic Ridge (Lerner et al. 2017), where hydrothermal vents were observed to release Fe-rich particles into the lower water column (Hayes et al. 2015b; Lam et al. 2015). Although the cause of enhanced scavenging in the deep water column may be different between these two regions, a model including an external particulate source, as the one considered in this study, could potentially also be used to quantify the impact of hydrothermal plumes on the scavenging of ^{230}Th and ^{231}Pa in the water column.

b. Budgets of ^{230}Th and ^{231}Pa in the BNL

In this section, we use the results from the model fit to data for GT11-04 and GT11-08 to establish tentative budgets of ^{230}Th and ^{231}Pa in the BNL at stations GT11-04 and GT11-08, thereby disentangling the roles of particle scavenging and physical transport. Specifically, the particle concentrations, radionuclide activities, and cycling parameters which are estimated from the fit are used to estimate the fluxes of turbulent mixing, radioactive production, particle settling, adsorption, desorption, as well as the strength of sediment source for each radionuclide at each station.

1) Dissolved ^{230}Th and ^{231}Pa

The terms in the budgets for dissolved ^{230}Th and ^{231}Pa are the radioactive production, the rates of adsorption and desorption, and the divergence of the turbulent mixing flux (Eq. 4a). Consider first the budgets for station GT11-04 (**Fig. 11**). In the region far above the BML (above about 300 m.a.b.), all fluxes are relatively small in magnitude. Below this region and in the BML (below 100 m.a.b.), the fluxes increase greatly in magnitude, except for radioactive production, which is uniform. For both radionuclides, the dissolved phase is primarily determined by a balance between adsorption and desorption, with relatively small contributions from turbulent mixing and radioactive production. The relatively small contribution from radioactive production is consistent with water column ^{230}Th budgets which have been estimated from data collected (i) at several locations in the western North Atlantic (Murnane et al. (1994); their Fig. 5) and (ii) at station GT11-22 east of the Mid-Atlantic Ridge (Lerner et al. (2016); their Fig. 17). Likewise, turbulent mixing is a relatively small term in the ^{230}Th$_d$ and ^{231}Pa$_d$ budgets. In the BML, the effect of turbulent mixing is overcome by the large adsorption fluxes caused by the abundance of particles and by the large desorption fluxes caused by the supply of ^{230}Th$_p$ and ^{231}Pa$_p$ from the particle source. Accordingly, the

dissolved phase is largely determined by sorption processes, with vertical mixing playing a secondary role. Similar results hold for station GT11-08 (**Fig. 12**). These results suggest that dissolved ^{230}Th and ^{231}Pa in the deep BNL at both stations are governed chiefly by interactions with resuspended sediment, which may have been diagenetically altered (Costa et al. 2020).

2) Particulate ^{230}Th and ^{231}Pa

The terms in the budgets for particulate ^{230}Th and ^{231}Pa are the rates of adsorption and desorption, the divergences of the turbulent mixing flux and of the particle settling flux, and the particle source (Eq. 4b). Consider again first the budgets for station GT11-04 (**Fig. 11**). Three different regions of the deep water column could be distinguished. In the upper region (> about 300 m.a.b.), the fluxes are relatively small in magnitude. In the intermediate region (approximately 20–300 m.a.b.), the magnitude of mixing, settling, and particle source terms are much larger, whereas the sorption fluxes, albeit larger than in the region above, are relatively small. Finally, in the lower region near the bottom (< about 20 m.a.b.), the very large particle source is mostly balanced by the divergence of the turbulent mixing flux, which exceeds that of the particle settling flux. As with the dissolved activity budgets, similar results hold for station GT11-08 (**Fig. 12**). Overall, these findings suggest that, different from the dissolved phase, the elevated levels of particulate ^{230}Th and ^{231}Pa in the deep BNL are governed chiefly by a balance among sediment redistribution, particle settling, and turbulent mixing, with sorption processes exerting a secondary control. Such a finding can potentially explain the difficulty of previous models (Rempfer et al. 2017; Gu and Liu 2017; van Hulten et al. 2018; Lerner et al. 2020; Sasaki et al. 2021), which lack an explicit representation of sediment redistribution, to reproduce deep water ^{230}Th and ^{231}Pa measurements in both phases simultaneously.

c. Paleoceanographic Implications

1) ^{230}Th Normalization

Measurements of the ^{230}Th activity of bulk sediment samples are used for correcting fluxes of sedimentary constituents for the effect of sediment redistribution by bottom currents, thereby allowing their interpretation in terms of particle fluxes from overlying surface waters (vertical rain rate). The merits and limitations of this method – called ^{230}Th normalization – have been reviewed by François et al. (2004) and Costa et al. (2020). A basic assumption of the method is that the settling flux of scavenged ^{230}Th to the seafloor is equal to the radioactive production rate of ^{230}Th in the overlying water column. This assumption has been shown to hold approximately from observations with sediment traps (e.g., Yu et al. (2001)) and from simulations

with circulation models (e.g., Henderson et al. (1999)).

An argument can be put forward that sediment resuspension in BNLs may not significantly alter the accuracy of the ^{230}Th normalization method in oceanic areas characterized by small topographic variations (François et al. 2004). Under the basic assumption of the method, the vertical rain rate of particles, F_p (e.g., in mg m^{-2} d^{-1}), could be estimated from

$$F_p = \frac{\beta_{\mathrm{Th}} D}{B_{s,\mathrm{Th}}}. \tag{15}$$

Here D is the local water depth, β_{Th} is the radioactive production rate of ^{230}Th, and $B_{s,\mathrm{Th}}$ is the excess ^{230}Th activity, i.e., the ^{230}Th activity of the sediment sample per mass of bulk dry sediment, corrected for ^{230}Th radioactive decay and for detrital and authigenic ^{230}Th (François et al. 2004). As argued by these authors, if particles that settle directly from the overlying waters (primary particles) and particles that are laterally redistributed have similar ^{230}Th activities, then ^{230}Th normalization as embodied by (15) would still be applicable. Such conditions would be met when sediment is redistributed over a relatively flat seafloor. Indeed, in this case, the ^{230}Th activity of primary and redistributed particles would be approximately similar, and sediment redistribution would not significantly change the ^{230}Th activity in focused sediments.

The ^{230}Th normalization method, however, may lead to biased results when applied at sediment core sites situated along, or adjacent to, continental slopes or similar reliefs (François et al. (2004); their section 4.6.2). For example, sediment core tops from the MAB showed excess ^{230}Th activities that increase about linearly with depth, from less than 1 dpm g^{-1} above 1000 m to more than 2–3 dpm g^{-1} below 2000 m (Anderson et al. (1994); **Fig. 9a**). As a result, sediment particles resuspended from the slope and rise, carried seaward by ocean currents, and deposited in deeper areas would tend to lower the excess ^{230}Th activity of sediment in these areas. Application of ^{230}Th normalization to sediment cores originating from these areas would thus lead to an overestimate of vertical rain rates.

Motivated by these considerations, we use our particle-radionuclide model to explore the influence of a lateral particle source on (i) the specific ^{230}Th activity of settling particles (activity per particle mass), C_p/C, and (ii) the vertical rain rate of particles, F_p (Eq. 15), with both quantities evaluated at the grid point just above the bottom. Both quantities (i)-(ii) are plotted as a function of the integrated particle source,

$$\langle j_c \rangle \equiv \int_0^H j_{c,o} e^{-z/\delta_r}\, dz = j_{c,o}\delta_r(1 - e^{-H/\delta_r}), \tag{16}$$

for different values of the ^{230}Th activity of source particles, B_r (**Fig. 13**). In these plots, the different values of B_r correspond to different water depths and are calculated from the regression of excess ^{230}Th of core tops from the MAB (**Fig. 9a**). The integrated particle source (Eq. 16) is set to vary from 0 to 4000 mg m^{-2} d^{-1}. This range is consistent with observational estimates of $\langle j_c \rangle \approx j_{c,o}\,\delta_r$ based on estimates of $j_{c,o}$ and δ_r

(section 3a). The other parameters of the model are held fixed and set equal to our posterior estimates for station GT11-04, on the New England continental rise, or station GT11-08, in the Hatteras abyssal plain (section 4b; **Table 3**). In our calculations, $\langle j_c \rangle$ is varied either by varying $j_{c,o}$ with δ_r fixed, or by varying δ_r with $j_{c,o}$ fixed; both cases yield very similar results (**Fig. 13**).

Consider first the results for GT11-04 (**Fig. 13**). We find that the specific ^{230}Th activity of settling particles, C_p/C, decreases by 1–5 dpm g^{-1} as the integrated particle source increases, depending on the depth from which source particles originate: source particles originating from shallower depths lead to a greater decrease than source particles originating from greater depths, as expected. As the integrated particle source increases, approaching 1000 mg m^{-2} d^{-1} and larger values, the specific ^{230}Th activity of settling particles approaches the specific ^{230}Th activity of source particles, showing that the activity of primary particles is overprinted by that of redistributed particles (**Fig. 13a**). The vertical rain rate of particles as calculated from equation (15) (with $B_{s,Th} = C_p/C$) increases with the integrated particle source, as expected from the fact that F_p is inversely proportional to $B_{s,Th}$: an increasing proportion near the seafloor of particulate matter resuspended from shallower depths, where B_r is lower, tends to produce larger estimates of vertical rain rate, in accordance with equation (15). The increase in vertical rain rate F_p with $\langle j_c \rangle$ ranges from 20 to 300 mg m^{-2} d^{-1}, depending on the water depth from which the source particles would originate (**Fig. 13b**).

Similar results are obtained for GT11-08 (**Fig. 13a–b**). For the posterior estimates of model parameters determined at this station, the specific ^{230}Th activity of particles near the seafloor decreases by 2–6 dpm g^{-1} as $\langle j_c \rangle$ increases, depending on the depth of the source particles. The vertical rain rate of particles increases by 15–400 mg m^{-2} d^{-1} as $\langle j_c \rangle$ increases in the same range, with particles resuspended from shallower depths leading to greater rain rate estimates than particles entrained from greater depths.

Costa et al. (2020) pointed out that the sources of particles (resuspension of sediments or lateral transport of material from surrounding topographic highs) should be identified in order to fully assess the accuracy of ^{230}Th normalization in regions where BNLs are present. To examine and illustrate this point, we plot the radionuclide activities in particles near the seafloor, their ratio, and ^{230}Th-normalized rain rate as calculated by the model against the mean PM concentration in the bottom 10 m of the water column (**Fig. 14**). As the mean PM concentration increases, driven by an increased particle source strength, ^{230}Th normalized rain rate also increases; such an increase is more prominent with mean PM concentration < 200 mg m^{-3} (**Fig. 14b**). Similarly, the shallower the depth from which source particles originate, the greater the apparent increase in vertical rain rate. Consistent with Costa et al. (2020), this result suggests that, when interpreting ^{230}Th normalized rain rate in regions characterized by lateral sediment transport, the source of particles would need to be identified, and that PM concentration in deep waters could be measured as a means to assess the

potential of sediment transport to bias estimates of vertical rain rate.

Overall, our results indicate that the resuspension and transport of sediment from the continental slope and rise can significantly alter the ^{230}Th activity of surficial sediments in deeper regions where the sediment is re-deposited. These results provide a quantitative illustration of the processes first described qualitatively by François et al. (2004). Sediment resuspension and transport processes combined may lead to a strong overestimation of ^{230}Th-corrected vertical rain rates in these regions, although the degree of overestimation would depend on a number of factors, such as the strength and vertical distribution of the particle source ($j_{C,0}$ and δ_r), the depths where particles are resuspended and thus the activity of the resuspended particles (B_r), the intensity of vertical turbulent mixing (κ_z), and the sorptive properties of the resuspended material (k_1 and k_{-1}). Our finding extends the studies of François et al. (2004) and Costa et al. (2020) by quantifying the potential bias imposed by sediment resuspension and transport on ^{230}Th-normalized fluxes.

2) Sediment ^{231}Pa/^{230}Th as a Paleoceanographic Indicator

In section 5a, we showed that the budgets of particulate ^{230}Th and ^{231}Pa in the BNL can be significantly influenced by an external particle source. Moreover, in the previous section, the ^{230}Th activity of particles near the seafloor was shown to vary significantly with both the strength of the particle source and the ^{230}Th activity of the source particles. These findings can have important implications for the interpretation of ^{231}Pa/^{230}Th records generated from sediment cores. In particular, the ^{231}Pa/^{230}Th ratio of particles settling at the top of the BNL may be 'mixed' with the ^{231}Pa/^{230}Th ratio of resuspended sediment being supplied laterally to the BNL. As a result, the ^{231}Pa/^{230}Th ratio of the underlying sediment may reflect oceanic conditions that prevailed, not at the core site, but at remote locations.

Here our particle-radionuclide model is applied to explore the sensitivity of the ^{231}Pa/^{230}Th ratio of particles near the bottom to the integrated particle source, $\langle j_c \rangle$, for source particles originating from different depths and thus characterized by different specific activities, B_r. As in the previous section, the integrated particle source is set to vary from 0 to 4000 mg m^{-2} d^{-1}, and the source particles originate from water depths ranging from 500 m to 3500 m (for GT11-04) or 4500 m (for GT11-08). As with ^{230}Th, the specific ^{231}Pa activity of source particles is calculated from the depth of origin of source particles by using the regression of excess ^{231}Pa data from the MAB (**Fig. 9b**; Anderson et al. (1994)). The values of the other model parameters are fixed to their posterior estimates for GT11-04 or GT11-08 (section 4b; **Table 3**). As in the previous section, $\langle j_c \rangle$ is varied either by varying $j_{c,o}$ with δ_r fixed, or by varying δ_r with $j_{c,o}$ fixed; both cases again yield very similar results (**Fig. 13**).

Consider first the results for GT11-04. As $\langle j_c \rangle$ increases, the specific ^{231}Pa activity of near-bottom

particles approaches the specific ^{231}Pa activity of source particles. The particulate ^{231}Pa is less sensitive to $\langle j_c \rangle$ if particles come from water depths that are closer to the local water depth (**Fig. 13c**). The ^{231}Pa/^{230}Th ratio of near-bottom particles increases as the integrated particle source increases: it varies from approximately 0.045 to about 0.090, depending on the depth from which source particles originate; source particles originating from shallower depths lead to a greater ^{231}Pa/^{230}Th variation than source particles originating from greater depths. The increase of particulate ^{231}Pa/^{230}Th with $\langle j_c \rangle$ is nonlinear and is negligible at large values of $\langle j_c \rangle$ (**Fig. 13d**). Similar results are obtained for GT11-08 (**Fig. 13c–d**). As expected, the particulate ^{231}Pa/^{230}Th increases similarly with the mean PM concentration in the bottom 10 m of the water column (**Fig. 14c–d**).

In summary, our calculations suggest that an external particle source may significantly influence the ^{231}Pa/^{230}Th ratio of near-bottom particles, depending on factors such as the strength of the particle source and the specific activities of the source particles. According to our calculations, the change in particulate ^{231}Pa/^{230}Th near the seafloor with $\langle j_c \rangle$ may be 0.015 or higher. A change of this magnitude is not negligible compared to the range of ^{231}Pa/^{230}Th values of suspended particles in the North Atlantic (Hayes et al. 2015b) and to the range of ^{231}Pa/^{230}Th values in Atlantic sediment records for the last deglaciation (for a recent compilation, see Ng et al. (2018)), the last glacial period (Henry et al. 2016), and the last glacial inception (e.g., Guihou et al. (2010, 2011)). Our results therefore suggest that, for sediment cores raised near continental slopes, rises, and similar topographic reliefs, ^{231}Pa/^{230}Th of bulk dry sediment may not only reflect the oceanic conditions that prevailed at the core site but also conditions at shallower depths. In fact, according to our calculations, the ^{231}Pa/^{230}Th ratio of particles deposited on the seabed predominantly reflects the ^{231}Pa/^{230}Th ratio of source particles, if the particle source is sufficiently strong.

d. Model Limitations

1) One-Dimensionality

The present model explicitly accounts for transport processes only in the vertical direction; the lateral supplies of particles and of particulate radionuclides are represented only implicitly through the source terms j_C (Eq. 2) and $B_r j_C$ (Eq. 4b), whereas the effect of horizontal transport on the dissolved activities is neglected altogether. Analysis of hydrographic data shows that different water masses, including DSOW, ISOW, CLSW, and AABW, were present below 3000 m at the investigated stations (section 4a). Conceivably, the transport of particles, ^{231}Pa, and ^{230}Th in these different water masses could have contributed to the observed vertical distribution of these properties at GA03 stations. In fact, evidence for an influence of lateral transport on PM distribution is apparent at a number of GA03 stations, although this influence may

not have been associated with deep water masses such as listed above. Thus, the presence of PM maxima well above the BML (**Fig. 4**), where vertical mixing rates are relatively low, may reflect the lateral transport of resuspended material from remote locations, rather than the upward mixing of locally-entrained sediment (e.g., McCave (1986)). At the deep stations investigated in this work (i.e., GT11-03 through GT11-10), θ and S profiles show a number of step changes in the stratified region above the BML, some of which appear to correspond to similar features in particle concentration profiles (e.g., GT11-10). Such correspondence, previously noticed in the Sohm abyssal plain, may reflect the lateral intrusion at mid-depth of bottom turbid layers detached from nearby topography (e.g., Armi (1978); McCave (1983)). In our model, the lateral transport of particles (and of particulate radionuclides) is represented through a particulate source.

Lateral supply of particles appears to be plausible at station GT11-04, where the BNL is the strongest among the stations considered in this study. Station GT11-04 (water depth 3772 m) is in slightly deeper water than the deepest DWBC velocity core at 3700 dbar as determined by 10 years of observations along line W (Toole et al. (2017); their Fig. 2a) and is located a short distance (about 10 km) southwest of a deep incision along the continental rise (**Fig. 1**). Inspection of a high-resolution bathymetric map of the western North American margin (Tucholke 1987) suggests that the incision may be the Veatch Canyon. A comprehensive study on the slope of southern MAB showed that sediment resuspension in canyons occur frequently, and that canyons can serve both as a conduit for downslope transport of shelf-derived material, and as a reservoir of sediments resuspended by breaking internal waves and transported to other locations (Biscaye and Anderson 1994). It seems conceivable that particles have been resuspended within the nearby canyons, such as the Veatch Canyon, from internal wave activity as postulated for the Baltimore Canyon (Gardner et al. 1983), and then transported to GT11-04 by the DWBC, thereby contributing to the elevated PM levels measured at that station.

Note that particles settling at a speed of 5.8 m d^{-1} from the top of the BNL would be able to travel over relatively large distances before their deposition to the seafloor. Current meters deployed in the western North Atlantic at different locations (including east of Bermuda Rise) and heights above the seabed (3.5 to 50 m.a.b.) recorded speeds that often exceed 5 cm s^{-1} (Gardner et al. 2017; their Figs. 2 to 5). Particles settling at a speed of 5.8 m d^{-1} from the top of a 500-m thick water column could travel over a horizontal distance of approximately 370 km if the horizontal velocity of the current amounts to 5 cm s^{-1} (Gardner et al. 1985a; their Fig. 7). The travel distance would range from about 360 km (370 km $\times$ 482/500) to 1000 km (370 km $\times$ 1358/500), based on our BNL thickness estimates along line W (Table 1); it could be much larger during episodes of intense sediment resuspension event, which seem to require a near-bottom current speed of about 20 cm s^{-1} (Gardner et al. 2017). Although bottom current speed varies with location and time, these results are consistent with our implicit assumption that particles settling at a speed of 5.8 m d^{-1}

can be supplied laterally from distant sources in the western North Atlantic.

2) Steady State Assumption

The steady state assumption in the model implies a strict balance between (vertical) transport processes on the one hand and sources and sinks on the other hand. With a particle settling speed of 5.8 m d^{-1}, the value assumed in our model, the estimated residence time of particles in a 600-m (800-m) thick BNL would be 103 days (138 days). An important question is whether perturbations exist in the deep sea that would be frequent and/or intense enough to prevent sediments and radionuclides at abyssal depths to reach steady state distributions on this time scale.

Evidence for such perturbations exists in the western North Atlantic, where episodic events of strong abyssal currents and intense BNL development have long been observed (e.g., Gardner and Sullivan (1981)). These "benthic storms" were studied in great detail offshore of the Nova Scotia continental rise during HEBBLE (McCave et al. 1988). Time series from nephelometers placed at 1 and 38 m.a.b. in the western North Atlantic recorded high PM events with levels estimated to 300-4000 mg m^{-3}, well above background levels of generally < 200 mg m^{-3}, and lasting 6-8 days (see synthesis of Gardner et al. (2017)). Deep-sea storms might be caused by synoptic events in the atmosphere such as hurricanes (e.g., Gardner and Sullivan (1981)) or result from the instability of the Gulf Stream (e.g., Gardner et al. (2017)). Interestingly, the GT11 cruise report stipulates that stormy weather conditions were experienced after GT11-04, with a hurricane passing between the ship and Bermuda, followed by three more days of sustained winds > 25 knots (Boyle et al. 2015). More generally, abyssal events such as benthic storms indicate that caution should be exercised in the application of steady-state models to interpret profiles of particle concentration and adsorption-prone elements in the deep western North Atlantic and perhaps in other oceanic regions as well.

3) Particle Dynamics

In this study, a single class of particles with a uniform settling speed is assumed, following Rutgers van der Loeff and Boudreau (1997). Although the assumption of uniform w_p appears justified for a preliminary investigation, the settling speed of particles is likely to vary through the deep water column, if particles present variable densities, sizes, and shapes (Hill and McCave 2001). Consequently, the assumption of uniform w_p may be questionable even in a model representing only a single class of particles. For example, McCave (1983) found that particle size spectra in the BNLs of HEBBLE area exhibited "a unimodal form with a peak at ~ 4 μm in high concentrations near the seabed changing to a bimodal form with an additional mode at ~ 16 μm in low concentrations high above the bed (500 and 1000 m.a.b.)". The author further

wrote that "the presence of the coarse mode at 1000 m.a.b. coupled with its increase in the lower 250 m of the water column suggests that it both settles from the surface and is resuspended from the bed" (McCave 1983). The particle size of 20 μm assumed in our model and based on Gardner et al. (1985a) is broadly consistent to the coarse mode but exceeds the peak of the fine mode reported by McCave (1983).

Perhaps more importantly, since only a single class of particles is represented in our model, processes of particle aggregation and particle disaggregation are not considered (McCave 1984; Burd and Jackson 2009). Particle aggregation is thought to be an important process for the removal of particles from the water column, as it tends to increase particles sizes and accelerate particle settling (e.g. McCave (1984)). A particle with a diameter of $\mathcal{O}(10\ \mu\text{m})$ can coalesce with other particles through Brownian motion, differential settling, and velocity shear, where the relative influence of each of these processes varies with the size of the interacting particle (e.g. McCave (1984)). In particular, the capture of fine particles by larger, faster sinking particles has been pointed out as a potential process for clearing BNLs (e.g. Hill and Nowell (1990); Thomsen and McCave (2000)). More complete models should consider at least two particle classes with second-order aggregation (Burd 2013). Ultimately, size spectrum models, which include a mechanistic description of particle coagulation phenomena, should be applied (Burd and Jackson 2009).

4) Sorption Kinetics

Particle scavenging of ^{231}Pa and ^{230}Th in our model increases with PM concentration through the adsorption rate constant (Eq. 5). Although this treatment is supported by theoretical considerations (e.g., Honeyman and Santschi (1989)) and observational evidence (e.g., Lerner et al. (2017)), it neglects the effect of other factors such as particle composition. Previous studies showed that particle composition may impact the solid-solution partitioning of ^{231}Pa and ^{230}Th (Hayes et al. 2015b) as well as the sorption kinetics of Th isotopes (Lerner et al. 2018) at stations occupied along the GA03 transect. Notably, the ^{231}Pa and ^{230}Th distribution coefficients associated with Fe and Mn (oxyhydr)oxides have been estimated to exceed those for the other major particle phases by at least one order of magnitude (Hayes et al. 2015b). This observation, combined with the fact that MnO_2 and to a lesser extent $Fe(OH)_3$ presented relatively large concentrations in the 1-51 μm size fraction in deep waters northwest of Bermuda (Lam et al. (2015); their Fig. 9), suggests that Pa and Th scavenging might have been enhanced in these waters due to the abundance of Fe and Mn (oxyhydr)oxides. Clearly, a more detailed description of particle scavenging in BNLs would need to consider the effect of particle type in addition to the effect of particle abundance.

6. Summary

In this study, we have examined the cycling of ^{231}Pa and ^{230}Th in benthic nepheloid layers. First, a brief analysis of hydrographic, optical, and radionuclide measurements collected along the GA03 transect between Woods Hole and Bermuda has been presented. We found, from high-resolution profiles of θ and S obtained from CTD casts, that waters at depths greater than about 3000 m could be described as mixtures of at least three water masses: DSOW, ISOW, and CLSW. The high silicate concentrations of these waters suggest that AABW was also present. A bottom mixed layer, with nearly-uniform values of θ and S and with thickness ranging from 95 to 320 m, was identified at all deep stations (GT11-04, 06, 08, and 10). Visual evidence for detached BMLs was found, particularly at station GT11-10 southeast of Bermuda. From high-resolution profiles of light attenuation, we determined that a strong BNL, with a thickness varying from 482 m to 1358 m, was present at the deep stations. At each of these stations, the BNL was characterised by (i) a basal region, presenting c_p maxima and broadly coinciding with the BML, and (ii) an upper region above the BML, presenting c_p levels generally decreasing with height above the seafloor and extending up to a clear water minimum at a depth between 2988 m and 3463 m. Using a regional calibration to convert c_p data into PM concentration estimates, we found a maximum PM level of about 2200 mg m^{-3} near the bottom at GT11-04, within the range of turbidity levels estimated from bottom-tethered nephelometers deployed in the western North Atlantic. Among the deep stations, the highest value of excess PM load was observed at GT11-04 on the continental rise, showing that the BNL was the most intense at this station.

Second, we have developed a simplified model of the cycling of PM, ^{230}Th, and ^{231}Pa in a BNL that is created by a lateral particle source from the resuspension and transport of sediment. We found that the model can reproduce the high particle concentrations, the low dissolved ^{230}Th and ^{231}Pa activities, and the high particulate ^{230}Th and ^{231}Pa activities, observed at stations GT11-04 and GT11-08, where samples were collected near the bottom for radionuclide analyses. A model fit to PM, ^{230}Th, and ^{231}Pa data reveals that the second-order rate constant of adsorption and the first-order rate constant of desorption are lower for both ^{230}Th and ^{231}Pa in the BNL than in other oceanic environments. These results suggest that a lateral particle source could account for the ^{230}Th and ^{231}Pa anomalies measured at abyssal depths in the western North Atlantic, thereby explaining the difficulty of ocean models lacking sediment resuspension to reproduce activity measurements in the two phases simultaneously. Budgets for ^{230}Th and ^{231}Pa in the BNL at GT11-04 and GT11-08 suggest that, at heights less than about 300 m.a.b., the dissolved phase is governed primarily by sorption reactions, whilst the particulate phase behaves primarily as a conservative constituent, supplied laterally and transported vertically by turbulent mixing and gravitational settling.

Finally, according to our model, the ^{230}Th and ^{231}Pa activities of particles near the seafloor vary sig-

nificantly with the strength of particle source integrated over the BNL, resulting in (i) an overestimate of ^{230}Th-corrected vertical rain rate and (ii) an increase in ^{231}Pa/^{230}Th ratio of particles settling to the seafloor. The changes in ^{231}Pa/^{230}Th of near-bottom particles caused by changes in the strength of the particle source are comparable to those observed in sediment ^{231}Pa/^{230}Th records during past climate changes. These results highlight the potential biases introduced by sediment redistribution near oceanic margins, complicating the application of ^{230}Th normalization and the interpretation of sediment ^{231}Pa/^{230}Th records, for cores raised from near continental slopes and similar reliefs.

Overall, our results suggest that the processes of sediment resuspension and lateral transport likely play a significant role in the cycling of ^{230}Th and ^{231}Pa in BNLs near oceanic margins. Future progress in this research would require a larger database: future field programs should focus on the generation of high-resolution profiles of particle concentration, particle composition, and radionuclide activities in the BNL, paired with analyses of sediment core tops, in different size fractions and in contrasting environments. More comprehensive models should consider the effect of circulation, departures from steady state, and more detailed treatments of particle dynamics and sorption kinetics. While our study suggests that resuspended sediment can significantly influence ^{230}Th and ^{231}Pa activities of particles settling to the seafloor, the implications of sediment redistribution for the paleoceanographic interpretation of sediment ^{230}Th and ^{231}Pa records remain to be further elucidated.

Acknowledgements

We thank Robert Anderson (LDEO), Kassandra Costa (WHOI), Wilford Gardner (UT Austin), Tristan Horner (WHOI), Stephanie Kienast (Dalhousie U.), Phoebe Lam (UCSC), Jerry McManus (LDEO), Hong Chin Ng (Bristol), Delia Oppo (WHOI), and David Thornalley (UCL) for discussions and constructive feedbacks. Wilford Gardner provided helpful comments on the manuscript, and Phoebe Lam clarified the approach used to constrain BNL thickness in a previous study. Detailed and constructive comments from three anonymous reviewers have allowed us to considerably improve the manuscript. This study was supported by the Woods Hole Oceanographic Institution through the Summer Fellowship Program, the U.S. National Sciences Foundation, and the MIT–WHOI Joint Program in Oceanography, Applied Ocean Science and Engineering. The cruise management for the GA03 transect was funded by the U.S. NSF and the European Research Council. Radionuclide studies were supported by the U.S. NSF.

Appendix A: Calibration of C vs C_p based on GA03 data

In this appendix, we attempt to establish a calibration of suspended PM concentration as a function of the beam attenuation coefficient for particles (c_p) by using data obtained from GA03 stations GT11-01 to GT11-10. The suspended PM data come from Lam et al. (2015) and the c_p data come from Schlitzer et al. (2018). Our calibration (**Fig. A1**) uses only PM concentrations measured at depths where the lithogenic fraction of PM exceeds 40%, consistent with the lithogenic fraction observed within the BNL at GA03 stations (Lam et al. (2015); their Fig. 10c). Beam attenuation data, which are available at high vertical resolution ($\sim$ 1 m), are linearly interpolated to the depths of PM data. The linear regression (ordinary least-square fit) of PM concentration against c_p yields

$$\mathrm{PM} = 2129 \cdot c_p - 47, \tag{A1}$$

where PM is in mg m^{-3} and c_p is in m^{-1}, with a squared coefficient of correlation $r^2 = 0.86$ ($n = 67$). Our PM-c_p calibration appears to be strongly influenced by three PM values > 200 mg m^{-3} (**Fig. A1**). When these high PM data are removed, the regression is dramatically altered ($\mathrm{PM} = 713 \cdot c_p - 1.92$), and the squared coefficient of correlation is reduced to $r^2 = 0.53$ ($n = 64$), which question the robustness of (A1). Moreover, the number of PM data > 200 mg m^{-3} ($n = 3$) is much smaller than that available to establish the calibration based on HEBBLE data ($n > 80$; Gardner et al. (1985b); their Fig. 10). Based on these results, the calibration of Gardner et al. (1985b) is used in this work.

Appendix B: Numerical Solution

In this appendix, we describe the numerical method used for solving the steady-state version (with $\partial/\partial t = 0$) of the governing equations for (i) the PM concentration (C) (main text Eq. 2) and (ii) the radionuclide activities in dissolved and particulate forms (C_d and C_p) (main text Eqs. 4a-b). As a result of the steady-state assumption, the partial differential equations (main text Eqs. 2 and 4a-b) reduce to ordinary differential equations (ODEs).

Our model domain extends from the seafloor at $z = 0$ to the top of BNL at $H = 600$ m (station GT11-04) or $H = 800$ m (station GT11-08) above the seafloor. It is represented by a regular grid with spacing $\Delta z = 1$ m between grid points. A total number of $n_w = 600$ grid points (station GT11-04) or $n_w = 800$ grid points (station GT11-08) indexed with $i = 1, \ldots, n_w$ are set in the domain. The point closest to seafloor ($i = 1$) is at $z = \Delta z/2 = 0.5$ m and the point farthest from the seafloor ($i = n_w$) is at $z = H - \Delta z/2$. The grid points $i = 1, \ldots, n_w$ carry the values of C, C_d, and C_p, whereas the interfaces midway between these points carry the values of κ_z.

The numerical method used for solving the ODEs of the model is based on finite differences. The ODEs for C, C_d, and C_p are approximated by difference equations that apply at the grid points of the model domain. The difference equations used to approximate the ODEs are based on a central difference scheme and are described below.

a. Discretization

First, the ODE for the PM concentration (main text Eq. 2) is approximated with the difference equation

$$\frac{1}{\Delta z}(\Phi_{i+1/2} - \Phi_{i-1/2}) = j_{c,o} e^{-z_i/\delta_r}. \tag{B1}$$

Here z_i is the height of grid point i above the seafloor, and $\Phi_{i+1/2}$ ($\Phi_{i-1/2}$) represents the settling and diffusive fluxes midway between grid points i and $i+1$ ($i-1$),

$$\Phi_{i+1/2} = w_p \frac{C_i + C_{i+1}}{2} - \kappa_{z,i+1/2} \frac{C_{i+1} - C_i}{\Delta z}, \tag{B2a}$$

$$\Phi_{i-1/2} = w_p \frac{C_{i-1} + C_i}{2} - \kappa_{z,i-1/2} \frac{C_i - C_{i-1}}{\Delta z}. \tag{B2b}$$

Equations (B2a) and (B2b) are used for all grid points with the following exceptions to accommodate the boundary conditions. The lower boundary condition (main text Eq. 7) is implemented as

$$\Phi_{i-1/2} = w_p C_i - 0, \tag{B3}$$

where $i = 1$, while the upper boundary condition (main text Eq. 6) is implemented as

$$\Phi_{i+1/2} = w_p \frac{C_i + C_H}{2} - \kappa_{z,i-1/2} \frac{C_H - C_i}{\Delta z}, \tag{B4}$$

when $i = n_w$. Note that the implementation of the upper boundary condition implies that C is not specified precisely at $z = H$ but at $z = H + \Delta z/2$ in the numerical model (a similar treatment applies to C_d and C_p; see below).

Second, the ODE for the dissolved radionuclide activity (main text Eq. 4a) is approximated as

$$\frac{1}{\Delta z}(\Phi_{i+1/2} - \Phi_{i-1/2}) = \beta + k_{-1} C_{p,i} - k_{1,i} C_{d,i}, \tag{B5}$$

where $k_{1,i} = k_{1,c} C_i$ and

$$\Phi_{i+1/2} = -\kappa_{z,i+1/2} \frac{C_{d,i+1} - C_{d,i}}{\Delta z}, \tag{B6a}$$

$$\Phi_{i-1/2} = -\kappa_{z,i-1/2} \frac{C_{d,i} - C_{d,i-1}}{\Delta z}. \tag{B6b}$$

Similarly, equations (B6a) and (B6b) apply to all grid points with two exceptions: at $i = 1$, the grid point nearest to the lower boundary, $\Phi_{i-1/2} = 0$ (main text Eq. 9a), and at $i = n_w$, the grid point nearest to the upper boundary, $\Phi_{i+1/2}$ is given by equation (B6a) with $C_{d,i+1} = C_{d,H}$.

Last, the ODE for the particulate radionuclide activity (main text Eq. 4b) is approximated as

$$\frac{1}{\Delta z}(\Phi_{i+1/2} - \Phi_{i-1/2}) = k_{1,i}C_{d,i} - k_{-1}C_{p,i} + j_{c,o}B_r e^{-z_i/\delta_r}, \tag{B7}$$

where

$$\Phi_{i+1/2} = w_p \frac{C_{p,i} + C_{p,i+1}}{2} - \kappa_{z,i+1/2}\frac{C_{p,i+1} - C_{p,i}}{\Delta z}, \tag{B8a}$$

$$\Phi_{i-1/2} = w_p \frac{C_{p,i-1} + C_{p,i}}{2} - \kappa_{z,i-1/2}\frac{C_{p,i} - C_{p,i-1}}{\Delta z}. \tag{B8b}$$

Equations (B8a) and (B8b) apply to all grid points with two exceptions: at $i = 1$, the grid point nearest to the lower boundary, $\Phi_{i-1/2} = w_p C_{p,i} - 0$ (main text Eq. 9b), and at $i = n_w$, the grid point nearest to the upper boundary, $\Phi_{i+1/2}$ is given by equation (B8a) with $C_{p,i+1} = C_{p,H}$.

b. Solution

The difference equations for C (B1), C_d (B5), and C_p (B7) together with their respective boundary conditions (Eqs. B3–B4, B6, and B8), constitute a system of algebraic equations which is solved in two steps. First, equation (B1) with boundary conditions (B3)-(B4) are written in the matrix-vector form

$$\mathbf{A}\mathbf{x} = \mathbf{b}, \tag{B9}$$

where the n_w-dimensional vector $\mathbf{x}$ includes the PM concentration at the different grid points (C_i), $\mathbf{A}$ is a $n_w \times n_w$ coefficient matrix, and $\mathbf{b}$ is a n_w-dimensional vector including (i) the particle sources at different grid points ($j_{c,o}e^{-z_i/\delta_r}$) and (ii) the PM concentration at the top of the BNL (C_H). The system (B9) is solved for $\mathbf{x}$, i.e., for C_i ($i = 1, \ldots, n_w$), using LU decomposition followed by substitutions (e.g., Strang et al. (1993)). The apparent first-order rate constant at the different grid points of the water subdomain is then calculated from $k_{1,i} = k_{1,c}C_i$.

Subsequently, equations B5 and B7 with their boundary conditions are cast together in a form similar to (B9). For this second problem, $\mathbf{x}$ is a $(2n_w)$-dimensional vector including the radionuclide activities (^{230}Th or ^{231}Pa) in dissolved form ($C_{d,i}$) and particulate form ($C_{p,i}$) at different grid points of the domain, $\mathbf{A}$ is a $2n_w \times 2n_w$ coefficient matrix, and $\mathbf{b}$ is a $2n_w$-dimensional vector including the radioactive production rate (β) and the boundary conditions at $z = H$ ($C_{d,H}$ and $C_{p,H}$). The resulting system $\mathbf{A}\mathbf{x} = \mathbf{b}$ is solved for $C_{d,i}$ ($i = 1, \ldots, n_w$) and $C_{p,i}$ ($i = 1, \ldots, n_w$) using again LU decomposition followed by substitutions.

Appendix C: Inverse Problem

In this appendix, we describe the inverse method (ATI) which is used to fit the equations of the particle-radionuclide model to the particle and radionuclide concentration data for GA03 stations GT11-04 and

GT11-08.

c. Formulation of the Inverse Problem

The model is fit to the data by adjusting the concentrations and the parameters of the model, so that agreement with the data is achieved in the least-squares sense. The concentrations and parameters of the model which are adjusted are defined in a vector of unknowns, noted $\mathbf{x}$. Prior knowledge about the elements of $\mathbf{x}$, obtained from the concentration measurements at GA03 stations and from estimates of model parameters reported in the literature, are contained in another vector, noted $\mathbf{x_o}$. We then define $\mathbf{C_o}$ as the covariance matrix of $\mathbf{x_o}$: the diagonal elements of $\mathbf{C_o}$ are the variances of the errors in the elements of $\mathbf{x_o}$ and the off-diagonal elements of $\mathbf{C_o}$ are the covariances between these errors. In this study, the error variances in $\mathbf{C_o}$ are set equal to the square of the errors in the concentration measurements and in the prior estimates of model parameters, and the error covariances in $\mathbf{C_o}$ are set to zero. Finally, we express the difference equations of the model (Appendix B) in the compact form $\boldsymbol{f}(\mathbf{x}) = \mathbf{0}$, where $\mathbf{0}$ is a vector of zeros.

The inverse problem, which is to fit the model equations to the data, can then be formulated as follows,

$$\texttt{minimize } J = (\mathbf{x} - \mathbf{x_o})^{\intercal} \mathbf{C_o}^{-1} (\mathbf{x} - \mathbf{x_o}), \quad \texttt{subject to } \boldsymbol{f}(\mathbf{x}) = \mathbf{0}. \tag{C1}$$

Here J is an objective, or cost, function, which describes the model-data misfit, and superscript T denotes the vector transpose. Thus, an estimate of $\mathbf{x}$ (values of concentrations and parameters) is sought such that J is minimum, subject to the constrain that the model equations are perfectly satisfied. In the jargon of optimization theory, problem (C1) is a nonlinearly constrained optimization problem (e.g., Gill et al. (1982)). The nonlinear character of the problem stems from the fact that the elements of $\mathbf{x}$ appear as nonlinear combinations in $\boldsymbol{f}(\mathbf{x}) = \mathbf{0}$ (consider for example the parameters $j_{C,0}$ and δ_r, which are combined as $j_{C,0}\, e^{-z/\delta_r}$ in the equation for particle concentration). That the solution of (C1) is a least-squares solution is particularly apparent for the case where $\mathbf{C_o}$ is diagonal, as it is assumed in this study, Indeed, in this case, the objective function reduces to a sum of squares,

$$J = \sum_{i=1}^{n} \left(\frac{x_i - x_{o,i}}{\sigma_{o,i}}\right)^2, \tag{C2}$$

where x_i is the ith element of the vector $\mathbf{x}$, $x_{o,i}$ is the ith element of the vector $\mathbf{x_o}$, and $\sigma_{o,i}$ is the error of $x_{o,i}$.

d. Prior Estimates and Uncertainties

The vector $\mathbf{x_o}$ contains prior estimates of the unknowns in $\mathbf{x}$, and the matrix $\mathbf{C_o}$ contains along its diagonal the squared errors in these estimates. These prior estimates and their errors are obtained as

follows. The particle concentrations at model grid points are obtained by linearly interpolating the particle concentration data derived from beam transmissometry (section 2). Since these data are available at high vertical resolution (1 m), the error incurred by interpolation is assumed to be negligible, and the error in the interpolated values is subjectively set to 100 mg m^{-3}. The radionuclide activities at model grid points closest to the sample depths are set equal to the radionuclide activity data at these depths, and their errors are set equal to the reported errors in these data (Schlitzer et al. 2018). The radionuclide activities at the other model grid points are obtained by linear interpolation of the radionuclide activity data, and their errors are set equal to a relatively large value of 1 dpm m^{-3} for both ^{230}Th and ^{231}Pa and for both the dissolved and particulate phases. For model grid points deeper than the deepest sample, the radionuclide activity is extrapolated from the deepest data and its error is also set to 1 dpm m^{-3} for both the dissolved and particulate phases.

Prior values of model parameters and their errors are set equal to observational estimates reported in the literature (Table 2). A prior value of the sediment particle source at the seafloor of $j_{C,0} = 100 \pm 50$ mg m^{-3} d^{-1} is assumed from estimates of particle fluxes (section 3a). The vertical scale for the resuspension source is set to a prior value of $\delta_r = 100 \pm 50$ m, comparable to our estimates of BML thickness (Table 1). The vertical eddy diffusivities are set to prior values of $\kappa_{z,1} = 432$ m^2 d^{-1} and $\kappa_{z,2} = 43.2$ m^2 d^{-1} (i.e., 0.005 m^2 s^{-1} and 0.0005 m^2 s^{-1}, respectively), with an error of 216 m^2 d^{-1} and 21.6 m^2 d^{-1}, respectively. These values are within the wide ranges of observational estimates of (0.19-100)$\times 10^{-3}$ m^2 s^{-1} for $\kappa_{z,1}$ and (0.05-20)$\times 10^{-4}$ m^2 s^{-1} for $\kappa_{z,2}$, which were deduced from ^{222}Rn measurements in the deep water column at several locations in the western North Atlantic (Sarmiento and Biscaye 1986; their Table 2). The prior value for the second-order rate constant for ^{230}Th absorption is set to $k_{1,c}= 0.029 \pm 0.014$ m^3 mg^{-1} yr^{-1} based on an analysis of bulk particle and Th isotope concentration data for GA03 stations east of Bermuda (Lerner et al. 2017). The prior value of $k_{1,c}$ for ^{231}Pa is set to one tenth this value, i.e., to $k_{1,c} = 0.0029 \pm 0.0014$ m^3 mg^{-1} yr^{-1}, as a crude representation of the generally lower affinity of Pa compared to Th for marine particles (e.g., Moran et al. 2002; Hayes et al. 2015b). On the other hand, in the absence of contradictory evidence, the first-order desorption rate constant is set to the same prior value for both metals, i.e., $k_{-1} = 1.0 \pm 0.125$ yr^{-1} for both ^{230}Th and ^{231}Pa, consistent with a number of estimates for Th in the literature (see Marchal and Lam (2012) for a compilation). Finally, the radionuclide activity of resuspended material is set to a prior value of $B_r = 2.0 \pm 1.0$ dpm g^{-1} for ^{230}Th and $B_r = 0.150 \pm 0.075$ dpm g^{-1} for ^{231}Pa. These values are within the range of excess ^{230}Th and ^{231}Pa activity measurements on sediment core top and sediment trap samples above 2000 m along the continental slope of the Mid-Atlantic Bight (Anderson et al. 1994; their Tables 2, 3, and 4).

e. Solution of the Inverse Problem

The solution of the inverse problem (B1), noted $\widehat{\mathbf{x}}$, is obtained through an iterative approach in which the nonlinear functions in $\boldsymbol{f}(\widehat{\mathbf{x}})$ are linearized around the value of $\widehat{\mathbf{x}}$ from the previous iteration (Tarantola and Valette 1982),

$$\widehat{\mathbf{x}}_{k+1} = \mathbf{x}_o + \mathbf{C}_o\mathbf{F}_k^\intercal(\mathbf{F}_k\mathbf{C}_o\mathbf{F}_k^\intercal)^{-1}(\mathbf{F}_k[\widehat{\mathbf{x}}_k - \mathbf{x}_o] - \boldsymbol{f}_k). \tag{C3}$$

Here k is the iteration number, $\mathbf{F}_k$ is a matrix that contains the partial derivatives of the functions in $\boldsymbol{f}(\widehat{\mathbf{x}}_k)$ with respect to the elements of $\widehat{\mathbf{x}}_k$, and $\boldsymbol{f}_k \equiv \boldsymbol{f}(\widehat{\mathbf{x}}_k)$. The matrix $\mathbf{F}_k$ is constructed such that the element in the ith row and jth column of $\mathbf{F}_k$ is $\partial f_i/\partial x_j$ evaluated at $\mathbf{x} = \widehat{\mathbf{x}}_k$. In our study, the iteration is initiated at $\widehat{\mathbf{x}}_{k=0} = \mathbf{x}_o$ and is interrupted when the difference between the new estimate $\widehat{x}_{i,k+1}$ and the previous estimate $\widehat{x}_{i,k}$ is less than 1% of the value of $\widehat{x}_{i,k}$ for each ith estimate in $\widehat{\mathbf{x}}$.

The error covariance matrix of $\widehat{\mathbf{x}}$ is approximated from (Tarantola and Valette 1982),

$$\mathbf{C}_{k+1} = \mathbf{C}_o - \mathbf{C}_o\mathbf{F}_k^\intercal(\mathbf{F}_k\mathbf{C}_o\mathbf{F}_k^\intercal)^{-1}\mathbf{F}_k\mathbf{C}_o. \tag{C4}$$

The estimated error of the ith element of $\widehat{\mathbf{x}}_{k+1}$ is the square root of the ith element along the diagonal of $\mathbf{C}_{k+1}$.

REFERENCES

Anderson, R., M. Fleisher, P. Biscaye, N. Kumar, B. Dittrich, P. Kubik, and M. Suter, 1994: Anomalous boundary scavenging in the middle atlantic bight: evidence from ^{230}Th, ^{231}Pa, ^{10}Be and ^{210}Pb. *Deep Sea Research Part II: Topical Studies in Oceanography*, **41 (2-3)**, 537–561.

Armi, L., 1978: Some evidence for boundary mixing in the deep ocean. *Journal of Geophysical Research: Oceans*, **83 (C4)**, 1971–1979.

Bacon, M. P., 1984: Glacial to interglacial changes in carbonate and clay sedimentation in the Atlantic Ocean estimated from ^{230}Th measurements. *Isotope Geoscience*, **2**, 97–111.

Bacon, M. P. and R. F. Anderson, 1982: Distribution of thorium isotopes between dissolved and particulate forms in the deep sea. *J. Geophys. Res.*, **87**, 2045–2056.

Bacon, M. P. and M. M. Rutgers van der Loeff, 1989: Removal of thorium-234 by scavenging in the bottom nepheloid layer of the ocean. *Earth Planet. Sci. Lett.*, **92**, 157–164.

Biscaye, P. E. and R. F. Anderson, 1994: Fluxes of particulate matter on the slope of the southern middle atlantic bight: Seep-ii. *Deep Sea Research Part II: Topical Studies in Oceanography*, **41 (2-3)**, 459–509.

Biscaye, P. E. and S. L. Eittreim, 1977: Suspended particulate loads and transports in the nepheloid layers of the abyssal Atlantic Ocean. *Mar. Geol.*, **23**, 155–172.

Boss, E., C. R. Sherwood, P. Hill, and T. Milligan, 2018: Advantages and limitations to the use of optical measurements to study sediment properties. *Applied Sciences*, **8 (12)**, 2692.

Boudreau, B., 1997: A one-dimensional model for bed-boundary layer particle exchange. *Journal of Marine Systems*, **11 (3-4)**, 279–303.

Boudreau, B. P., 2001: Solute transport above the sediment-water interface. *The Benthic boundary layer: Transport processes and biogeochemistry*, 104–126.

Boudreau, B. P. and B. B. Jørgensen, 2001: The benthic boundary layer: Transport processes and biogeochemistry.

Boyle, E. A., R. F. Anderson, G. A. Cutter, R. Fine, W. J. Jenkins, and M. Saito, 2015: Introduction to the us geotraces north atlantic transect (GA-03): USGT10 and USGT11 cruises. *DSR-II*, **116**, 1–5.

Bulfinch, D. L. and M. T. Ledbetter, 1983: Deep western boundary undercurrent delineated by sediment texture at base of north american continental rise. *Geo-marine letters*, **3 (1)**, 31–36.

Burd, A. B., 2013: Modeling particle aggregation using size class and size spectrum approaches. *Journal of Geophysical Research: Oceans*, **118 (7)**, 3431–3443.

Burd, A. B. and G. A. Jackson, 2009: Particle aggregation. *Annu. Rev. Marine Sci.*, **1**, 65–90.

Cheng, H., et al., 2013: Improvements in ^{230}Th dating, ^{230}Th and ^{234}U half-life values, and U-Th isotopic measurements by multi-collector inductively coupled plasma mass spectrometry. *Earth Planet. Sci. Lett.*, **371-372**, 82–91.

Costa, K. M., et al., 2020: ^{230}Th normalization: New insights on an essential tool for quantifying sedimentary fluxes in the modern and quaternary ocean. *Paleoceanography and paleoclimatology*, **35 (2)**, e2019PA003 820.

Driscoll, M. L., B. E. Tucholke, and I. McCave, 1985: Seafloor zonation in sediment texture on the nova scotian lower continental rise. *Marine geology*, **66 (1-4)**, 25–41.

Eittreim, S., M. Ewing, and E. Thorndike, 1969: Suspended matter along the continental margin of the North American Basin. *Deep Sea Res.*, **16**, 613–624.

François, R., M. Frank, M. M. Rutgers van der Loeff, and M. P. Bacon, 2004: 230th normalization: An essential tool for interpreting sedimentary fluxes during the late quaternary. *Paleoceanography*, **19 (1)**.

Gardner, W., M. Richardson, K. Hinga, and P. Biscaye, 1983: Resuspension measured with sediment traps in a high-energy environment. *Earth and Planetary Science Letters*, **66**, 262–278.

Gardner, W., M.-J. Richardson, and A. Mishonov, 2018a: Global assessment of benthic nepheloid layers and linkage with upper ocean dynamics. *Earth Planet. Sci. Lett.*, **482**, 126–134.

Gardner, W., M.-J. Richardson, A. Mishonov, and P. Biscaye, 2018b: Global comparison of benthic nepheloid layers based on 52 years of nephelometer and transmissometer measurements. *Prog. Oceanogr.*, **168**, 100–111.

Gardner, W., J. Southard, and C. Hollister, 1985a: Sedimentation, resuspension and chemistry of particles in the northwest Atlantic. *Mar. Geol.*, **65**, 199–242.

Gardner, W. and L. Sullivan, 1981: Benthic storms: Temporal variability in a deep-ocean nepheloid layer. *Science*, **213**, 329–331.

Gardner, W., B. Tucholke, M.-J. Richardson, and P. Biscaye, 2017: Benthic storms, nepheloid layers, and linkage with upper ocean dynamics in the western North Atlantic. *Mar. Geol.*, **385**, 304–327.

Gardner, W. D., P. E. Biscaye, J. R. V. Zaneveld, and M. J. Richardson, 1985b: Calibration and comparison of the ldgo nephelometer and the osu transmissometer on the nova scotian rise. *Marine Geology*, **66 (1-4)**, 323–344.

Geibert, W. and R. Usbeck, 2004: Adsorption of thorium and protactinium onto different particle types: Experimental findings. *Geochim. Cosmochim. Acta*, **68**, 1489–1501.

Gill, P., W. Murray, and M. Wright, 1982: Practical optimization. publisher. Academic Press.

Gu, S. and Z. Liu, 2017: ^{231}Pa and ^{230}Th in the ocean model of the Community Earth System Model (CESM1.3). *Geosci. Model Dev.*, **10**, 4723–4742.

Guihou, A., S. Pichat, A. Govin, S. Nave, E. Michel, J.-C. Duplessy, P. Telouk, and L. Labeyrie, 2011: Enhanced atlantic meridional overturning circulation supports the last glacial inception. *Quaternary Science Reviews*, **30 (13-14)**, 1576–1582.

Guihou, A., S. Pichat, S. Nave, A. Govin, L. Labeyrie, E. Michel, and C. Waelbroeck, 2010: Late slowdown of the atlantic meridional overturning circulation during the last glacial inception: new constraints from sedimentary (^{231}Pa/^{230}Th). *Earth and Planetary Science Letters*, **289 (3-4)**, 520–529.

Hayes, C., et al., 2015a: ^{230}Th and ^{231}Pa on GEOTRACES GA03, the US GEOTRACES North Atlantic transect, and implications for modern and paleoceanographic chemical fluxes. *Deep Sea Res. II*, **116**, 29–41.

Hayes, C., et al., 2015b: Intensity of Th and Pa scavenging partitioned by particle chemistry in the North Atlantic Ocean. *Mar. Chem.*, **170**, 49–60.

Henderson, G. M., C. Heinze, R. F. Anderson, and A. M. E. Winguth, 1999: Global distribution of the ^{230}Th flux to ocean sediments constrained by GCM modelling. *Deep Sea Res. I*, **46**, 1861–1893.

Henry, L., J. McManus, W. Curry, N. Roberts, A. Piotrowski, and L. Keigwin, 2016: North atlantic ocean circulation and abrupt climate change during the last glaciation. *Science*, **353 (6298)**, 470–474.

Hill, P. and I. McCave, 2001: Suspended particle transport in benthic boundary layers. *The benthic boundary layer: Transport processes and biogeochemistry*, 78–103.

Hill, P. and A. Nowell, 1990: The potential role of large, fast-sinking particles in clearing nepheloid layers. *Phil. Trans. Roy. Soc., London A*, **331**, 103–107.

Honeyman, B. D., L. S. Balistrieri, and J. W. Murray, 1988: Oceanic trace metal scavenging: The importance of particle concentration. *Deep Sea Res.*, **35**, 227–246.

Honeyman, B. D. and P. H. Santschi, 1989: A Brownian-pumping model for oceanic trace metal scavenging: Evidence from Th isotopes. *J. Marine Res.*, **47**, 951–992.

Huang, P.-Q., X.-R. Cen, Y.-Z. Lu, S.-X. Guo, and S.-Q. Zhou, 2018: An integrated method for determining the oceanic bottom mixed layer thickness based on woce potential temperature profiles. *Journal of Atmospheric and Oceanic Technology*, **35 (11)**, 2289–2301.

Huang, P.-Q., X.-R. Cen, Y.-Z. Lu, S.-X. Guo, and S.-Q. Zhou, 2019: Global distribution of the oceanic bottom mixed layer thickness. *Geophysical Research Letters*, **46 (3)**, 1547–1554.

Jackett, D. R., T. J. McDougall, R. Feistel, D. G. Wright, and S. M. Griffies, 2006: Algorithms for density, potential temperature, conservative temperature, and the freezing temperature of seawater. *Journal of Atmospheric and Oceanic Technology*, **23 (12)**, 1709–1728.

Jeandel, C., M. R. van der Loeff, P. J. Lam, M. Roy-Barman, R. M. Sherrell, S. Kretschmer, C. German, and F. Dehairs, 2015: What did we learn about ocean particle dynamics in the GEOSECS–JGOFS era? *Progress in Oceanography*, **133**, 6–16.

Jenkins, W., W. Smethie Jr, E. Boyle, and G. Cutter, 2015: Water mass analysis for the US GEOTRACES (GA03) north atlantic sections. *Deep Sea Research Part II*, **116**, 6–20.

Jerome, S., et al., 2020: Half-life determination and comparison of activity standards of ^{231}Pa. *Applied Radiation and Isotopes*, **155**, 108 837.

Kretschmer, S., W. Geibert, M. M. Rutgers van der Loeff, C. Schnabel, S. Xu, and G. Mollenhauer, 2011: Fractionation of ^{230}Th, ^{231}Pa, and ^{10}Be induced by particle size and composition within an opal-rich sediment of the Atlantic Southern Ocean. *Geochim. Cosmochim. Acta*, **75**, 6971–6987.

Kretschmer, S., W. Geibert, M. M. R. van der Loeff, and G. Mollenhauer, 2010: Grain size effects on 230thxs inventories in opal-rich and carbonate-rich marine sediments. *Earth and Planetary Science Letters*, **294 (1-2)**, 131–142.

Kumar, N., R. Anderson, R. Mortlock, P. Froelich, P. Kubik, B. Dittrich-Hannen, and M. Suter, 1995: Increased biological productivity and export production in the glacial southern ocean. *Nature*, **378 (6558)**, 675–680.

Lam, P. J., D. C. Ohnemus, and M. E. Auro, 2015: Size-fractionated major particle composition and concentrations from the US GEOTRACES North Atlantic Zonal Transect. *Deep Sea Res. II*, **116**, 303–320.

Lavelle, J., H. Mofjeld, and E. Baker, 1984: An in situ erosion rate for a fine-grained marine sediment. *Journal of Geophysical Research: Oceans*, **89 (C4)**, 6543–6552.

Lerner, P., O. Marchal, P. Lam, K. Buesseler, and M. Charette, 2017: Kinetics of thorium and particle cycling along the U.S. GEOTRACES North Atlantic Transect. *Deep Sea Res.*, **125**, 106–128.

Lerner, P., O. Marchal, P. Lam, and A. Solow, 2018: Effects of particle composition on thorium scavenging in the North Atlantic. *Geochim. Cosmochim. Acta*, **233**, 115–134.

Lerner, P., O. Marchal, P. J. Lam, W. Gardner, M. J. Richardson, and A. Mishonov, 2020: A model study of the relative influences of scavenging and circulation on ^{230}Th and ^{231}Pa in the western north atlantic. *Deep Sea Research Part I: Oceanographic Research Papers*, **155**, 103 159.

Lerner, P., et al., 2016: Testing models of thorium and particle cycling in the ocean using data from station GT11-22 of the U.S. GEOTRACES North Atlantic section. *Deep Sea Res.*, **113**, 57–79.

Lorbacher, K., D. Dommenget, P. Niiler, and A. Köhl, 2006: Ocean mixed layer depth: A subsurface proxy of ocean-atmosphere variability. *Journal of Geophysical Research: Oceans*, **111 (C7)**.

Luo, Y., R. François, and S. Allen, 2010: Sediment ^{231}Pa/^{230}Th as a recorder of the Atlantic meridional overturning circulation: Insights from a 2-D model. *Ocean Sci.*, **6**, 381–400.

Marchal, O., R. François, and J. Scholten, 2007: Contribution of ^{230}Th measurements to the estimation of the abyssal circulation. *Deep Sea Res. I*, **54**, 557–585.

Marchal, O. and P. Lam, 2012: What can paired measurements of Th isotope activity and particle concentration can tell us about particle cycling in the ocean? *Geochim. Cosmochim. Acta*, **90**, 126–148.

McCave, I., 1983: Particulate size spectra, behavior, and origin of nepheloid layers over the nova scotian continental rise. *Journal of Geophysical Research: Oceans*, **88 (C12)**, 7647–7666.

McCave, I., 1984: Erosion, transport and deposition of fine-grained marine sediments. *Geological Society, London, Special Publications*, **15 (1)**, 35–69.

McCave, I., C. Hollister, and A. Nowell, 1988: *Deep Ocean Sediment Transport: Volume II: High Energy Benthic Boundary Layer Experiment: Collected Reprints of Office of Naval Research Funded Studies*. Woods Hole Oceanographic Institution.

McCave, I. N., 1986: Local and global aspects of the bottom nepheloid layers in the world ocean. *Neth. J. Sea Res.*, **20**, 167–181.

McDougall, T. J. and P. M. Barker, 2011: Getting started with teos-10 and the gibbs seawater (gsw) oceanographic toolbox. *SCOR/IAPSO WG*, **127**, 1–28.

McLean, S. R., 1985: Theoretical modelling of deep ocean sediment transport. *Marine geology*, **66 (1-4)**, 243–265.

Mengual, B., P. L. Hir, F. Cayocca, and T. Garlan, 2017: Modelling fine sediment dynamics: Towards a common erosion law for fine sand, mud and mixtures. *Water*, **9 (8)**, 564.

Moran, S. B., C.-C. Shen, H. N. Edmonds, S. E. Weinstein, J. N. Smith, and R. L. Edwards, 2002: Dissolved and particulate ^{231}Pa and ^{230}Th in the Atlantic Ocean: Constraints on intermediate/deep water age, boundary scavenging, and ^{231}Pa/^{230}Th fractionation. *Earth Planet. Sci. Lett.*, **203**, 999–1014.

Murnane, R. J., J. K. Cochran, K. O. Buesseler, and M. P. Bacon, 1996: Least-squares estimates of thorium, particle, and nutrient cycling rate constants from the JGOFS North Atlantic Bloom Experiment. *Deep Sea Res.*, **43**, 239–258.

Murnane, R. J., J. K. Cochran, and J. L. Sarmiento, 1994: Estimates of particle- and thorium-cycling rates in the northwest Atlantic Ocean. *J. Geophys. Res.*, **99**, 3373–3392.

Ng, H. C., L. F. Robinson, J. F. McManus, K. J. Mohamed, A. W. Jacobel, R. F. Ivanovic, L. J. Gregoire, and T. Chen, 2018: Coherent deglacial changes in western atlantic ocean circulation. *Nature communications*, **9 (1)**, 1–10.

Nozaki, Y., Y. Horibe, and H. Tsubota, 1981: The water column distributions of thorium isotopes in the western North Pacific. *Earth Planet. Sci. Lett.*, **54**, 203–216.

Nyffeler, U. P., Y.-H. Li, and P. H. Santschi, 1984: A kinetic approach to describe trace-element distribution between particles and solution in natural aquatic systems. *Geochim. Cosmochim. Acta*, **48**, 1513–1522.

Okubo, A., H. Obata, T. Gamo, and M. Yamada, 2012: 230th and 232th distributions in mid-latitudes of the north pacific ocean: Effect of bottom scavenging. *Earth and Planetary Science Letters*, **339**, 139–150.

Owens, S., S. Pike, and K. Buesseler, 2015: Thorium-234 as a tracer of particle dynamics and upper ocean export in the atlantic ocean. *Deep Sea Research Part II: Topical Studies in Oceanography*, **116**, 42–59.

Owens, S. A., K. O. Buesseler, and K. W. W. Sims, 2011: Re-evaluating the ^{238}U–salinity relationship in seawater: Implications for the ^{238}U–^{234}Th disequilibrium method. *Mar. Chem.*, **127**, 31–39.

Pavia, F., et al., 2018: Intense hydrothermal scavenging of ^{230}Th and ^{231}Pa in the deep Southeast Pacific. *Mar. Chem.*, **201**, 212–228.

Pavia, F. J., et al., 2019: Timescales of hydrothermal scavenging in the south pacific ocean from 234th, 230th, and 228th. *Earth and Planetary Science Letters*, **506**, 146–156.

Peine, F., R. Turnewitsch, C. Mohn, T. Reichelt, B. Springer, and M. Kaufmann, 2009: The importance of tides for sediment dynamics in the deep sea—evidence from the particulate-matter tracer 234th in deep-sea environments with different tidal forcing. *Deep Sea Research Part I: Oceanographic Research Papers*, **56 (7)**, 1182–1202.

Rempfer, J., T. Stocker, F. Joos, and J. Lippold, 2017: New insights into cycling of ^{231}Pa and ^{230}Th in the Atlantic Ocean. *Earth Planet. Sci. Lett.*, **468**, 27–37.

Roberts, K., C. Xu, C.-C. Hung, M. Conte, and P. Santschi, 2009: Scavenging and fractionation of thorium vs. protactinium in the ocean, as determined from particle-water partitioning experiments with sediment trap material from Gulf of Mexico and Sargasso Sea. *Earth Planet. Sci. Lett.*, **286**, 131–138.

Rutgers van der Loeff, M. M. and B. P. Boudreau, 1997: The effect of resuspension on chemical exchanges at the sediment - water interface in the deep sea - A modelling and natural radiotracer approach. *J. Marine Sys.*, **11**, 305–342.

Rutgers van der Loeff, M. M., R. Meyer, B. Rudels, and E. Rachor, 2002: Resuspension and particle transport in the benthic nepheloid layer and near Fram Strait in relation to faunal abundances and ^{234}Th depletion. *Deep Sea Res. I*, **49**, 1941–1958.

Ryan, W., et al., 2009: Global multi-resolution topography synthesis. *Geochem. Geophys. Geosys.*, **10**, Q03 014, doi: 10.1029/2008GC002 332.

Sarmiento, J. L. and P. E. Biscaye, 1986: Radon 222 in the benthic boundary layer. *Journal of Geophysical Research: Oceans*, **91 (C1)**, 833–844.

Sasaki, Y., H. Kobayashi, and A. Oka, 2021: An investigation into the processes controlling the global distribution of dissolved ^{231}Pa and ^{230}Th in the ocean and the sedimentary ^{231}Pa/^{230}Th ratios by using an ocean general circulation model coco ver4.0. *Geoscientific Model Development Discussions*, 1–37.

Schlitzer, R., et al., 2018: The GEOTRACES Intermediate Data Product 2017. *Chem. Geol.*, **493**, 210–223.

Smith, J. D., 1975: Modeling of sediment transport on continental shelves. Tech. rep., Washington Univ., Seattle (USA). Dept. of Oceanography.

Strang, G., G. Strang, G. Strang, and G. Strang, 1993: *Introduction to linear algebra*, Vol. 3. Wellesley-Cambridge Press Wellesley, MA.

Talley, L. D., 2011: *Descriptive physical oceanography: an introduction*. Academic press.

Tarantola, A. and B. Valette, 1982: Generalized nonlinear inverse problems solved using the least squares criterion. *Reviews of Geophysics*, **20 (2)**, 219–232.

Thomsen, L. and I. McCave, 2000: Aggregation processes in the benthic boundary layer at the celtic sea continental margin. *Deep Sea Research Part I: Oceanographic Research Papers*, **47 (8)**, 1389–1404.

Toole, J., M. Andres, I. Le Bras, T. Joyce, and M. McCartney, 2017: Moored observations of the Deep Western Boundary Current in the NW Atlantic: 2004–2014. *J. Geophys. Res. Oceans*, **122**, 7488–7505.

Tucholke, B., 1987: Submarine geology. *The Marine Environment of the U.S. Atlantic Continental Slope and Rise*, 56–113.

Turnewitsch, R. and B. M. Springer, 2001: Do bottom mixed layers influence ^{234}Th dynamics in the abyssal near-bottom water column? *Deep Sea Res.*, **48**, 1279–1307.

van Hulten, M., J.-C. Dutay, and M. Roy-Barman, 2018: A global scavenging and circulation ocean model of thorium-230 and protactinium-231 with realistic particle dynamics (NEMO-ProThorP 0.1). *Geosci. Model Dev.*, **11**, 3537–3556.

Wiberg, P. L., D. E. Drake, and D. A. Cacchione, 1994: Sediment resuspension and bed armoring during high bottom stress events on the northern california inner continental shelf: measurements and predictions. *Continental Shelf Research*, **14 (10-11)**, 1191–1219.

Xu, C., et al., 2011: Controls of 234th removal from the oligotrophic ocean by polyuronic acids and modification by microbial activity. *Marine Chemistry*, **123 (1-4)**, 111–126.

Yu, E.-F., R. François, M. P. Bacon, and A. Fleer, 2001: Fluxes of ^{230}Th and ^{231}Pa to the deep sea: Implications for the interpretation of excess ^{230}Th and ^{231}Pa/^{230}Th profiles in sediments. *Earth Planet. Sci. Lett.*, **191**, 219–230.

Yu, E.-F., R. Francois, and M. P. Bacon, 1996: Similar rates of modern and last-glacial ocean thermohaline circulation inferred from radiochemical data. *Nature*, **379**, 689–694.

List of Tables

1 Characteristics of the Deep Water Column along Line W GA03 Stations 49

2 Parameters of the Particle-Radionuclide Model 50

3 Least-Squares Estimates of Particle and Radionuclide Cycling Parameters [a] 51

Table 1: Characteristics of the Deep Water Column along Line W GA03 Stations

Station	Bottom Depth (m)	CWM [a] Depth (m)	Entire BNL [b] Thickness (m)	Strong BNL [b] Thickness (m)	QI [c]	BML [d] Thickness (m)	Excess PM [e] Load (mg m^{-2})
GT11-04	3772	2988	784	482	0.76	105	2×10^6
GT11-06	4582	3066	1516	1358	0.83	105	3×10^5
GT11-08	4926	3463	1463	730	0.90	95	4×10^5
GT11-10	4567	3244	1323	1031	0.73	320	1×10^4

[a] clear water minimum
[b] benthic nepheloid layer
[c] quality index
[d] bottom mixed layer
[e] particulate matter

Table 2: Parameters of the Particle-Radionuclide Model

w_p	particle settling velocity	-5.8 [a]	m d^{-1}
$\kappa_{z,1}$	vertical eddy diffusivity in BML	432 ± 216 [b]	m^2 d^{-1}
$\kappa_{z,2}$	vertical eddy diffusivity in upper BNL	43.2 ± 21.6 [b]	m^2 d^{-1}
$j_{C,0}$	particle source at the bottom	100 ± 50 [b]	mg m^{-3} d^{-1}
δ_r	height scale for particle source	100 ± 50 [b]	m
	^{230}Th		
β	radioactive production rate	2.52×10^{-2} [a]	dpm m^{-3} yr^{-1}
$k_{1,c}$	2nd-order rate constant for adsorption	0.029 ± 0.014 [b]	m^3 mg^{-1} yr^{-1}
k_{-1}	1st-order rate constant for desorption	1.0 ± 0.125 [b]	yr^{-1}
B_r	source particle activity	2.0 ± 1.0 [b]	dpm g^{-1}
	^{231}Pa		
β	radioactive production rate	2.33×10^{-3} [a]	dpm m^{-3} yr^{-1}
$k_{1,c}$	2nd-order rate constant for adsorption	0.0029 ± 0.0014 [b]	m^3 mg^{-1} yr^{-1}
k_{-1}	1st-order rate constant for desorption	1.0 ± 0.125 [b]	yr^{-1}
B_r	source particle activity	0.15 ± 0.075 [b]	dpm g^{-1}

[a] Fixed value.
[b] Prior value ± 1 standard deviation.

Table 3: Least-Squares Estimates of Particle and Radionuclide Cycling Parameters [a]

	Station GT11-04	Station GT11-08	
$\kappa_{z,1}$	155.6 ± 11.6	186.1 ± 41.9	$m^2\ d^{-1}$
$\kappa_{z,2}$	95.4 ± 16.2	35.4 ± 19.2	$m^2\ d^{-1}$
$j_{C,0}$	152.3 ± 4.7	57.9 ± 7.8	$mg\ m^{-3}\ d^{-1}$
δ_r	81.0 ± 2.4	50.5 ± 6.4	m
		^{230}Th	
$k_{1,c}$	0.0068 ± 0.0013	0.0038 ± 0.0005	$m^3\ mg^{-1}\ yr^{-1}$
k_{-1}	0.204 ± 0.050	0.052 ± 0.016	yr^{-1}
B_r	3.67 ± 0.11	6.96 ± 0.73	$dpm\ g^{-1}$
		^{231}Pa	
$k_{1,c}$	0.0022 ± 0.0003	0.0021 ± 0.0003	$m^3\ mg^{-1}\ yr^{-1}$
k_{-1}	0.908 ± 0.121	0.692 ± 0.115	yr^{-1}
B_r	0.302 ± 0.009	0.250 ± 0.026	$dpm\ g^{-1}$

[a] Posterior values $\pm$ 1 standard deviation.

List of Figures

1 Map of the western North Atlantic, with a yellow inset showing the continental slope and rise offshore New England, and a white inset showing the HEBBLE area (Gardner et al. 1985b). Red dots mark the locations of stations occupied along the U.S. GEOTRACES North Atlantic transect (GA03). White lines show the location of SEEP-I and SEEP-II transects (Anderson et al. 1994). Dotted lines with arrows represent the schematic pathways of major currents (Talley 2011); note that the actual pathways are both wider and more variable than illustrated. Also shown in the yellow inset are the location of sediment core tops from SEEP-I (green triangles) and deep canyon locations (bathymetric data from Ryan et al. (2009)). 55

2 Schematic of the model of particle, ^{230}Th, and ^{231}Pa cycling in the deep water column. The model includes elements of the reversible exchange model of Bacon and Anderson (1982) and of the model of particle exchange between the seabed and the benthic boundary layer of Rutgers van der Loeff and Boudreau (1997). 56

3 Scatter plot of potential temperature versus salinity for deep waters ($>$ 3000 m) at GA03 stations along line W. The potential density anomaly contours (in kg m^{-3}) are calculated by the Gibbs-Seawater Oceanographic Toolbox (TEOS-10) (McDougall and Barker 2011). The solid circles show values measured along CTD casts at stations GT11-03, 04, 06, 08, and 10 (data from Schlitzer et al. (2018)). The open circles show estimated values for Denmark Strait Overflow Water, Iceland-Scotland Overflow Water, and Classical Labrador Sea Water (Jenkins et al. (2015)). The estimated values of potential temperature (0.18°C) and salinity (34.702) for Antarctic Bottom Water (Jenkins et al. (2015)) are outside the range of displayed values. 57

4 Profiles of potential temperature (θ), salinity (S), and particulate matter (PM) concentration measured at GA03 stations (a) GT11-04, (b) GT11-06, (c) GT11-08, and (d) GT11-10. The yellow shaded area in each panel highlights the bottom mixed layer, where θ and S are relatively uniform (data from Schlitzer et al. (2018)). 58

5 Profiles of (a) PM concentration, (b) dissolved ^{230}Th and ^{231}Pa activities, and (c) particulate ^{230}Th and ^{231}Pa activities, at stations GT11-03, 04, 06, 08, and 10. Legend on the right applies to panels (b) and (c). The dotted colour lines mark the depth of clear water minimum (CWM) at each station. Note the logarithmic scale for the abscissa in panels (a) and (c) (data from Hayes et al. (2015a) and Schlitzer et al. (2018)). 59

6 Profiles of particulate matter (PM) concentration derived from measurements of the beam attenuation coefficient for particles (blue crosses) and the model fit to the PM data (red lines), in the benthic nepheloid layer at stations GT11-04 (left panel) and GT11-08 (right panel). Data of beam attenuation coefficient come from Schlitzer et al. (2018). 60

7 Measurements of dissolved and particulate ^{230}Th activities (blue circles), and the model fit to these measurements (red line), in the benthic nepheloid layer at stations GT11-04 (left panels) and GT11-08 (right panels). Error bars for the radionuclide data represent ± 2 standard deviations. The ^{230}Th data are from Hayes et al. (2015a). 61

8 Measurements of dissolved and particulate ^{231}Pa activities (blue circles), and the model fit to these measurements (red line), in the benthic nepheloid layer at stations GT11-04 (left panels) and GT11-08 (right panels). Error bars for the radionuclide data represent ± 2 standard deviations. The ^{231}Pa data are from Hayes et al. (2015a). 62

9 Excess ^{231}Pa and ^{230}Th data for sediment core tops from SEEP-I and SEEP-II transects in the Middle Atlantic Bight (Anderson et al. 1994). Panel a: Excess ^{231}Pa and excess ^{230}Th versus the water depth of the sediment cores. The dashed lines are the least-squares fits. Panel b: Scatter plot of excess ^{231}Pa versus excess ^{230}Th. The dashed line is the least-squares fit. In both panels, circles are from SEEP-I and triangles are from SEEP-II. 63

10 Profiles of k_1 for ^{230}Th (left panel) and ^{231}Pa (right panel) estimated from data inversion at GT11-04 and GT11-08. 64

11 Profiles of radionuclide fluxes in the BNL at station GT11-04 from data inversion. Discontinuities in the fluxes near the interface between the BML and the upper BNL ($z = 100$ m) are due to the different eddy diffusivities across the interface. 65

12 Profiles of radionuclide fluxes in the BNL at station GT11-08 from data inversion. Discontinuities in the fluxes near the interface between the BML and the upper BNL ($z = 100$ m) are due to the different eddy diffusivities across the interface. 66

13 Variations of (a) specific ^{230}Th activity of settling particles, (b) ^{230}Th-corrected particle rain rate, (c) specific ^{231}Pa activity of settling particles, and (d) ^{231}Pa/^{230}Th of settling particles with the integrated particle source ($\langle j_c \rangle$) for different particle source depths and thus different source activities. Solid lines show results obtained when $\langle j_c \rangle$ is varied by varying $j_{c,o}$ with δ_r fixed, whereas crosses show results obtained by varying δ_r with $j_{c,o}$ fixed. Left and right panels show variations calculated from posterior estimates of model parameters at stations GT11-04 (bottom depth 3772 m) and GT11-08 (bottom depth 4926 m), respectively. The inset on the right is a schematic showing different origins of source particles in relation to the water column. 67

14 Same as Figure 13, but plotted against mean PM concentration in the bottom 10 m of the water column. 68

15 Figure A1: Scatter plot of suspended PM concentration and beam attenuation coefficient (c_p) in deep water along the western margin in the North Atlantic. The black dots are data from GA03 stations GT11-01 to GT11-10 (Lam et al. 2015; Schlitzer et al. 2018). The solid red line is the least-squares fit for these data, and the dashed red line is the least squared fit for these data with the three PM > 200 mg m^{-3} values removed. As a reference, the calibration reported by Gardner et al. (1985b) based on HEBBLE data is also shown (blue). 69

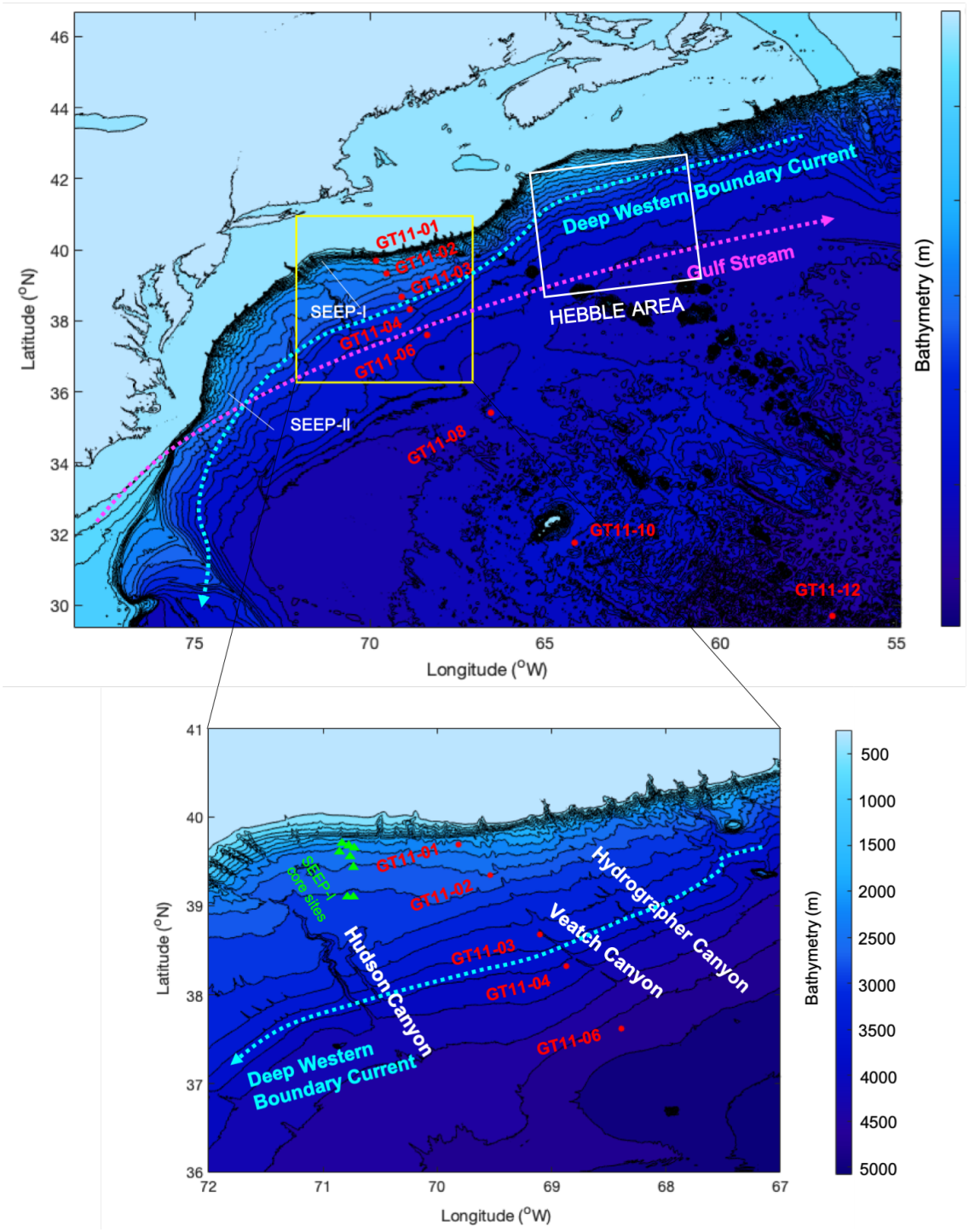

Figure 1: Map of the western North Atlantic, with a yellow inset showing the continental slope and rise offshore New England, and a white inset showing the HEBBLE area (Gardner et al. 1985b). Red dots mark the locations of stations occupied along the U.S. GEOTRACES North Atlantic transect (GA03). White lines show the location of SEEP-I and SEEP-II transects (Anderson et al. 1994). Dotted lines with arrows represent the schematic pathways of major currents (Talley 2011); note that the actual pathways are both wider and more variable than illustrated. Also shown in the yellow inset are the location of sediment core tops from SEEP-I (green triangles) and deep canyon locations (bathymetric data from Ryan et al. (2009)).

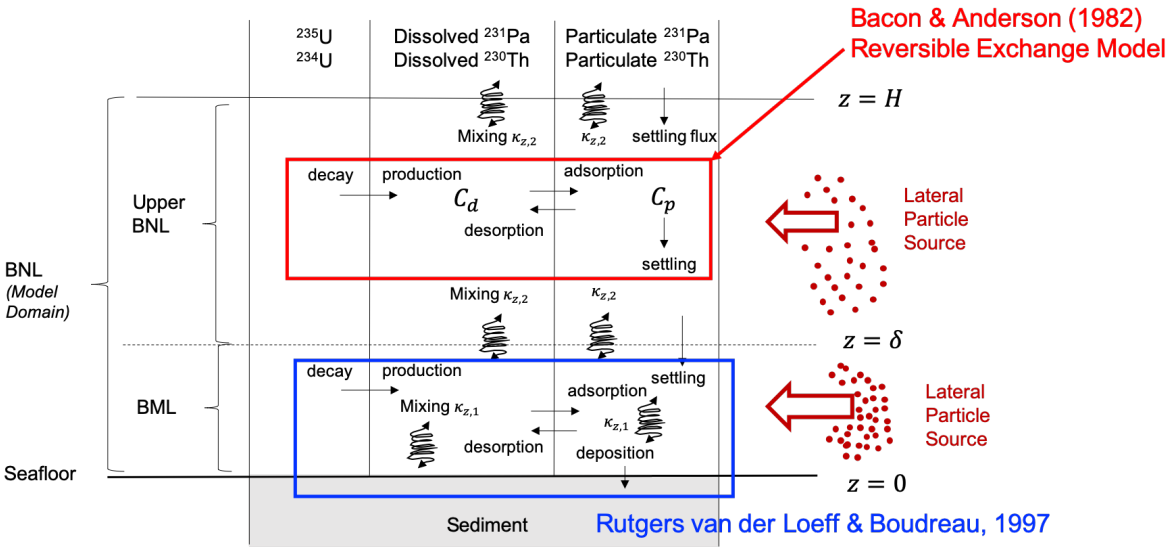

Figure 2: Schematic of the model of particle, ^{230}Th, and ^{231}Pa cycling in the deep water column. The model includes elements of the reversible exchange model of Bacon and Anderson (1982) and of the model of particle exchange between the seabed and the benthic boundary layer of Rutgers van der Loeff and Boudreau (1997).

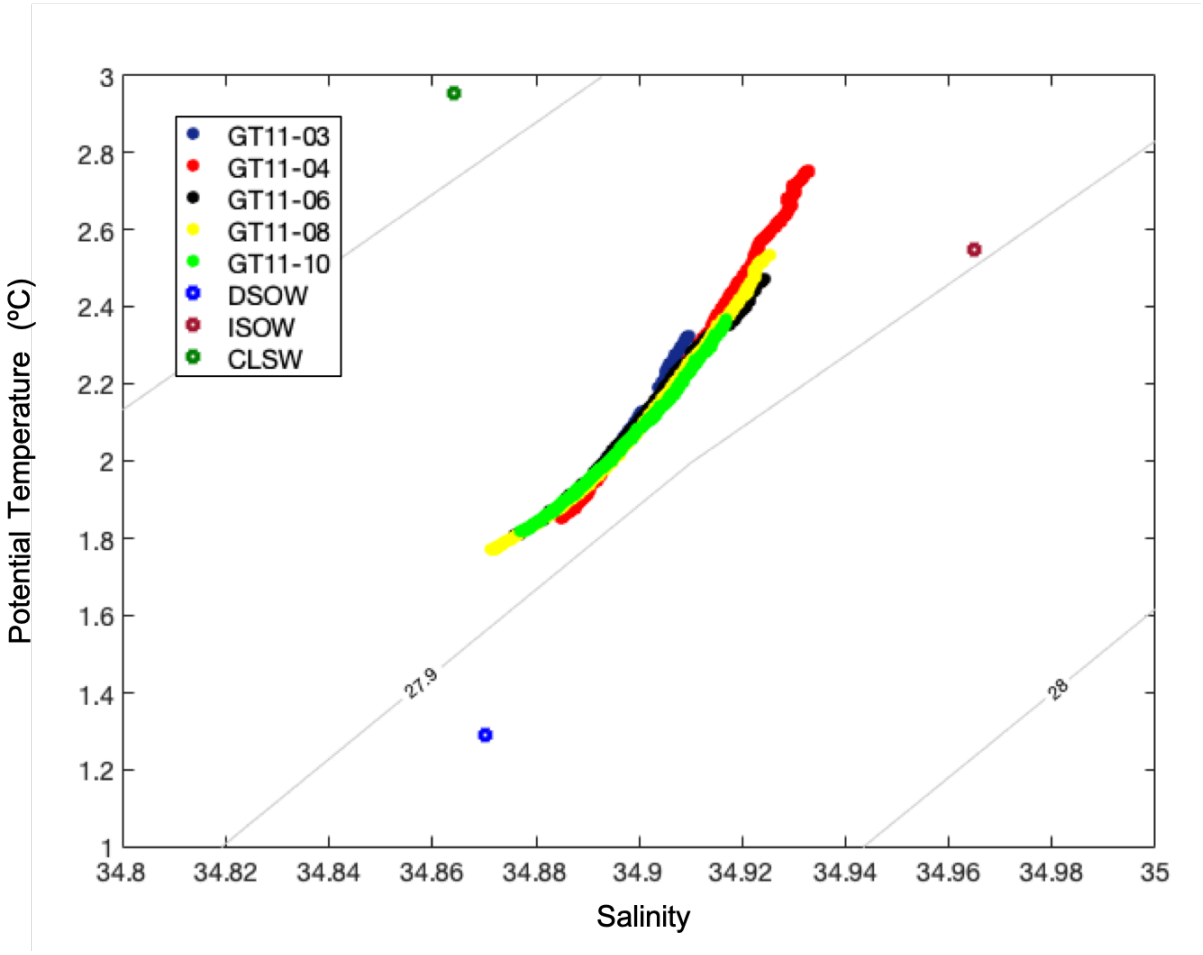

Figure 3: Scatter plot of potential temperature versus salinity for deep waters (> 3000 m) at GA03 stations along line W. The potential density anomaly contours (in kg m^{-3}) are calculated by the Gibbs-Seawater Oceanographic Toolbox (TEOS-10) (McDougall and Barker 2011). The solid circles show values measured along CTD casts at stations GT11-03, 04, 06, 08, and 10 (data from Schlitzer et al. (2018)). The open circles show estimated values for Denmark Strait Overflow Water, Iceland-Scotland Overflow Water, and Classical Labrador Sea Water (Jenkins et al. (2015)). The estimated values of potential temperature (0.18°C) and salinity (34.702) for Antarctic Bottom Water (Jenkins et al. (2015)) are outside the range of displayed values.

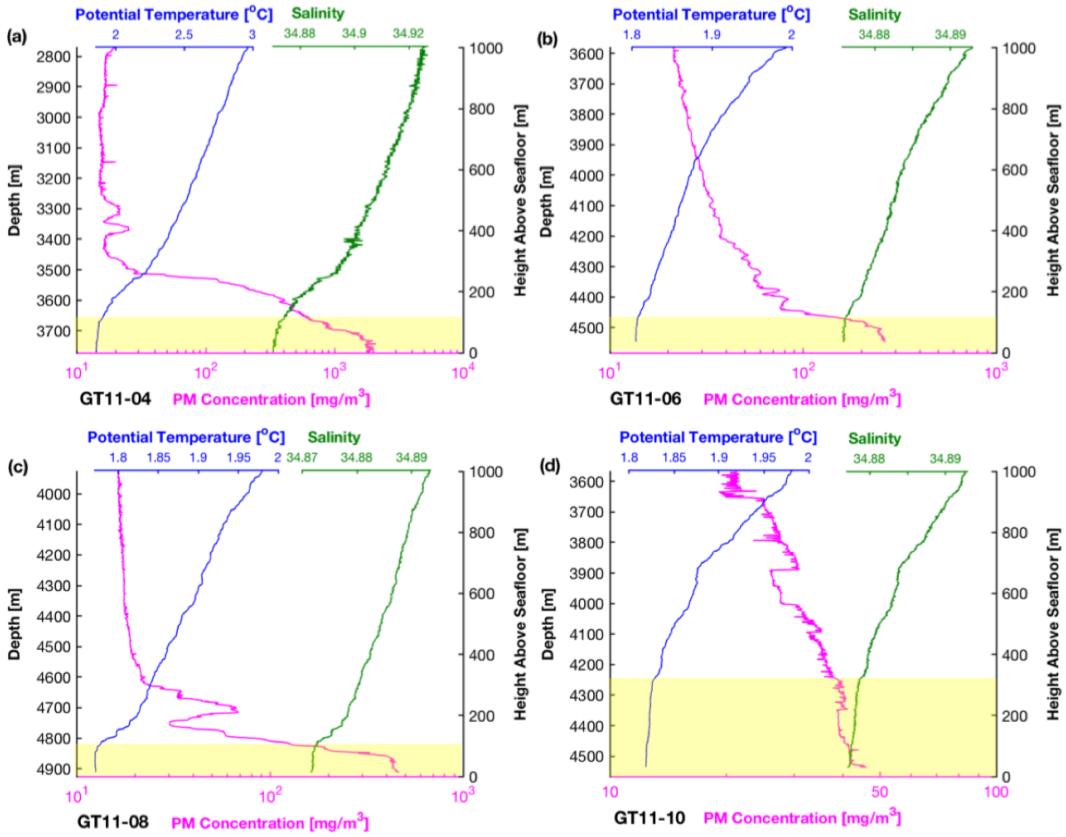

Figure 4: Profiles of potential temperature (θ), salinity (S), and particulate matter (PM) concentration measured at GA03 stations (a) GT11-04, (b) GT11-06, (c) GT11-08, and (d) GT11-10. The yellow shaded area in each panel highlights the bottom mixed layer, where θ and S are relatively uniform (data from Schlitzer et al. (2018)).

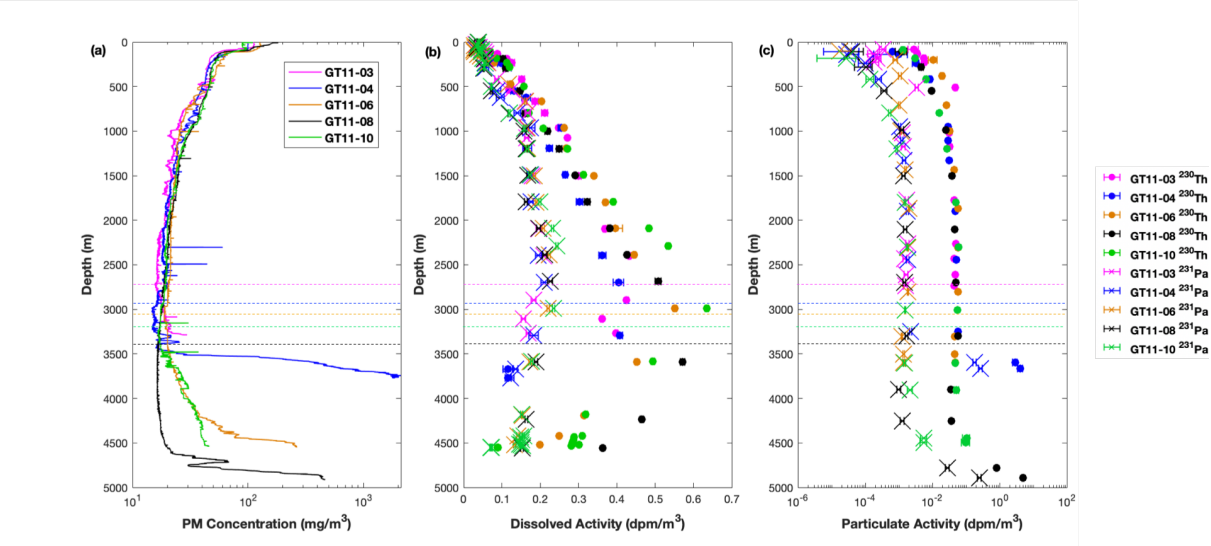

Figure 5: Profiles of (a) PM concentration, (b) dissolved ^{230}Th and ^{231}Pa activities, and (c) particulate ^{230}Th and ^{231}Pa activities, at stations GT11-03, 04, 06, 08, and 10. Legend on the right applies to panels (b) and (c). The dotted colour lines mark the depth of clear water minimum (CWM) at each station. Note the logarithmic scale for the abscissa in panels (a) and (c) (data from Hayes et al. (2015a) and Schlitzer et al. (2018)).

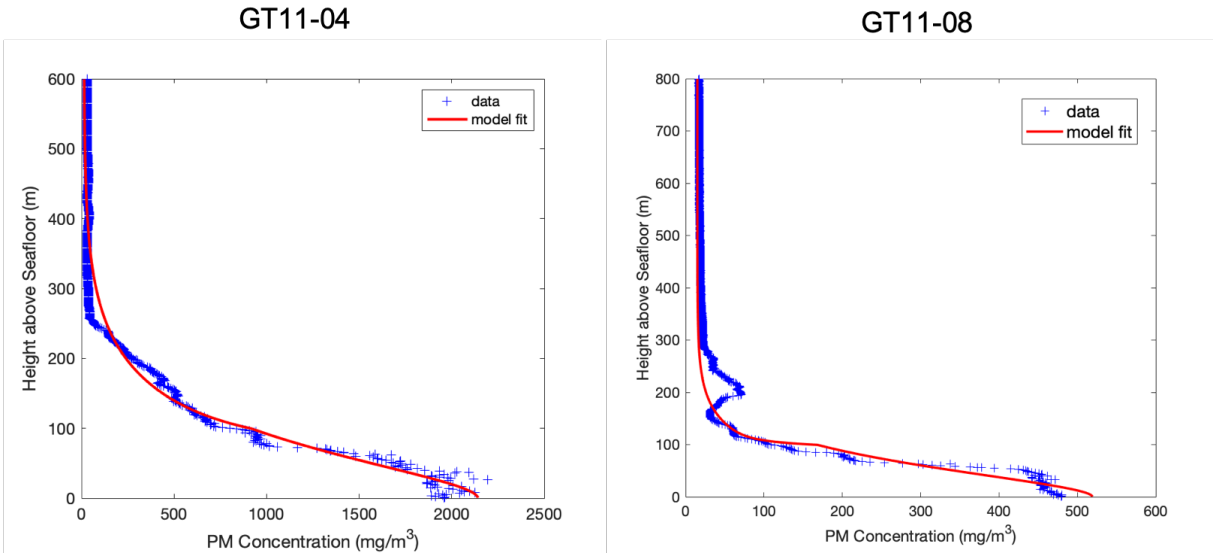

Figure 6: Profiles of particulate matter (PM) concentration derived from measurements of the beam attenuation coefficient for particles (blue crosses) and the model fit to the PM data (red lines), in the benthic nepheloid layer at stations GT11-04 (left panel) and GT11-08 (right panel). Data of beam attenuation coefficient come from Schlitzer et al. (2018).

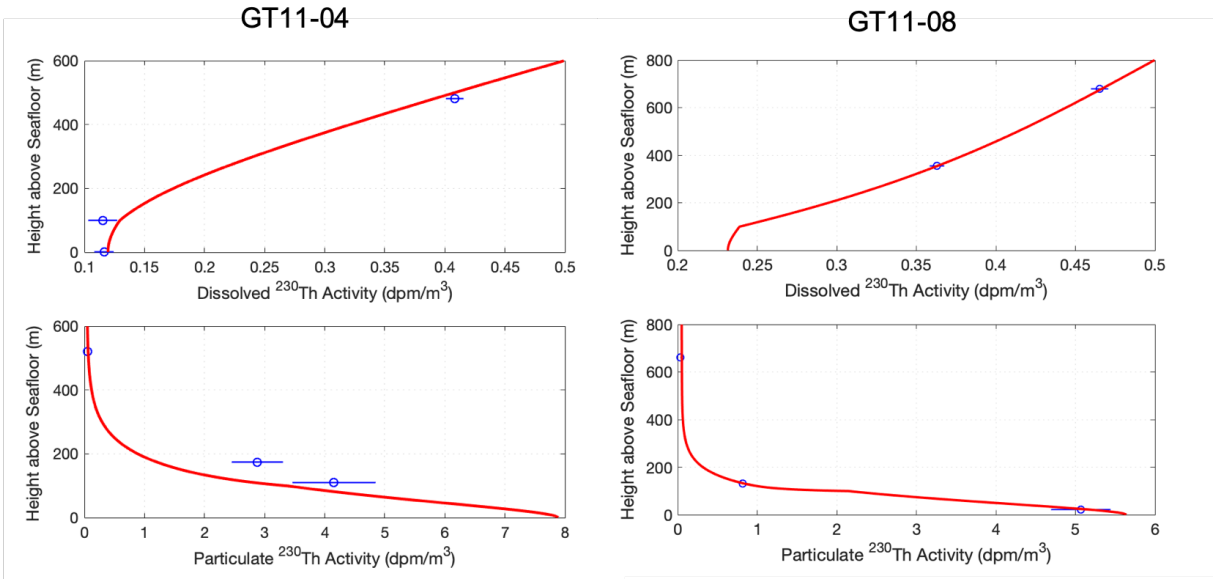

Figure 7: Measurements of dissolved and particulate ^{230}Th activities (blue circles), and the model fit to these measurements (red line), in the benthic nepheloid layer at stations GT11-04 (left panels) and GT11-08 (right panels). Error bars for the radionuclide data represent ± 2 standard deviations. The ^{230}Th data are from Hayes et al. (2015a).

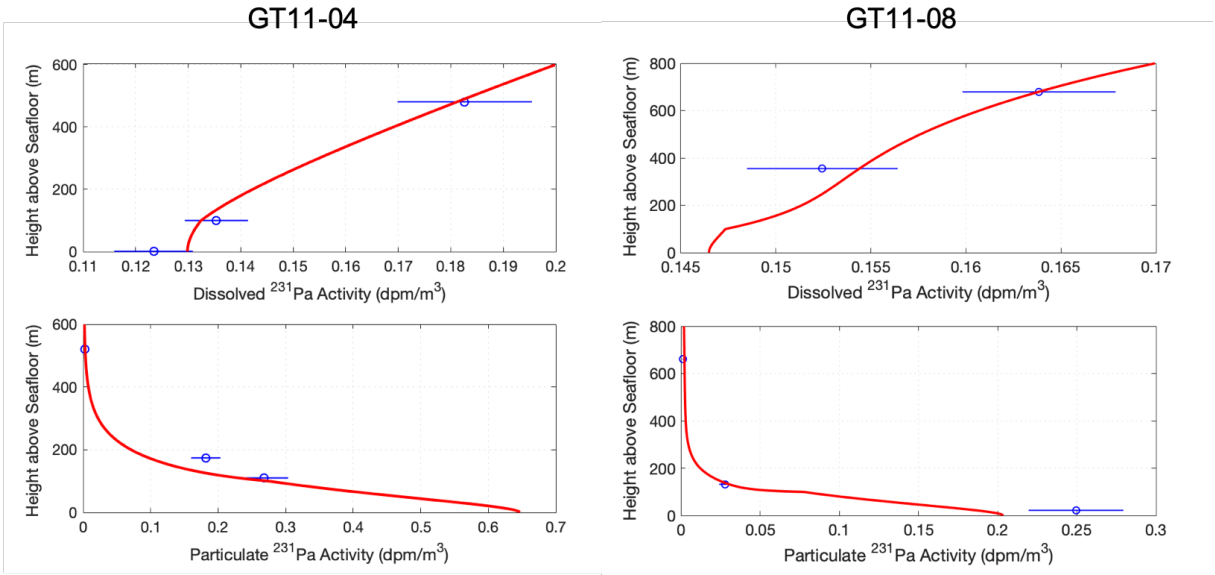

Figure 8: Measurements of dissolved and particulate ^{231}Pa activities (blue circles), and the model fit to these measurements (red line), in the benthic nepheloid layer at stations GT11-04 (left panels) and GT11-08 (right panels). Error bars for the radionuclide data represent ± 2 standard deviations. The ^{231}Pa data are from Hayes et al. (2015a).

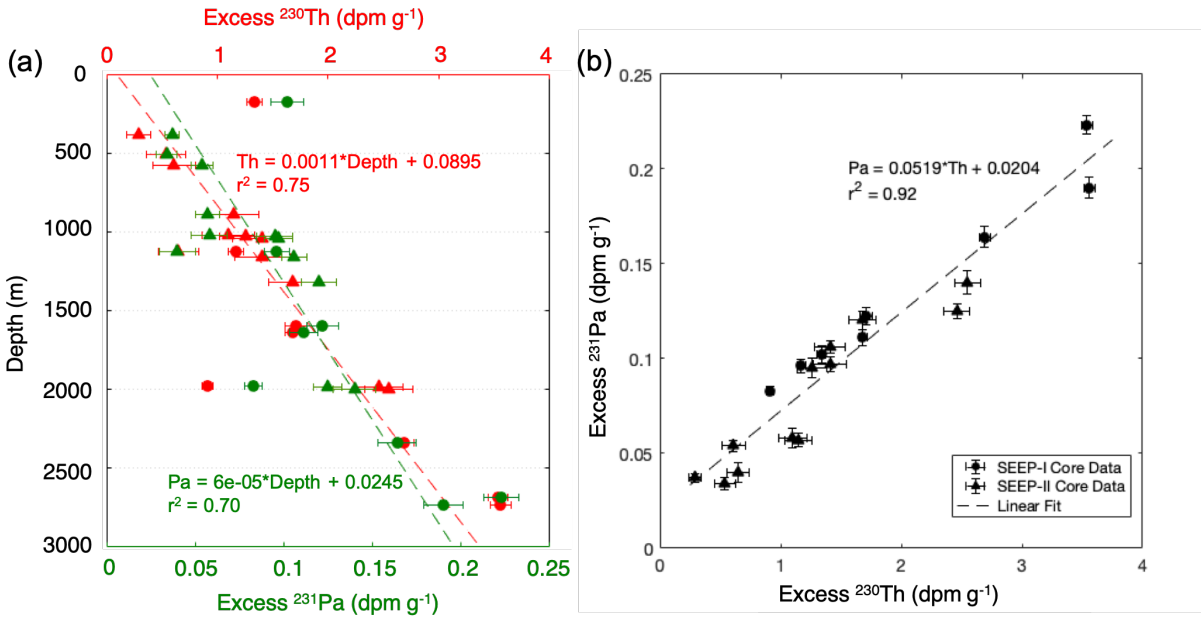

Figure 9: Excess ^{231}Pa and ^{230}Th data for sediment core tops from SEEP-I and SEEP-II transects in the Middle Atlantic Bight (Anderson et al. 1994). Panel a: Excess ^{231}Pa and excess ^{230}Th versus the water depth of the sediment cores. The dashed lines are the least-squares fits. Panel b: Scatter plot of excess ^{231}Pa versus excess ^{230}Th. The dashed line is the least-squares fit. In both panels, circles are from SEEP-I and triangles are from SEEP-II.

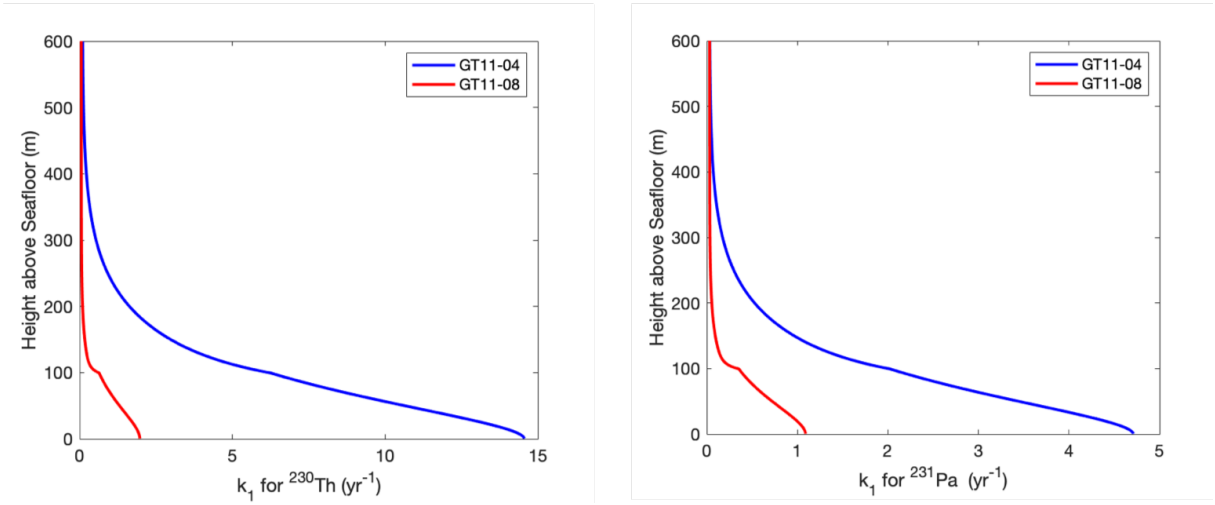

Figure 10: Profiles of k_1 for ^{230}Th (left panel) and ^{231}Pa (right panel) estimated from data inversion at GT11-04 and GT11-08.

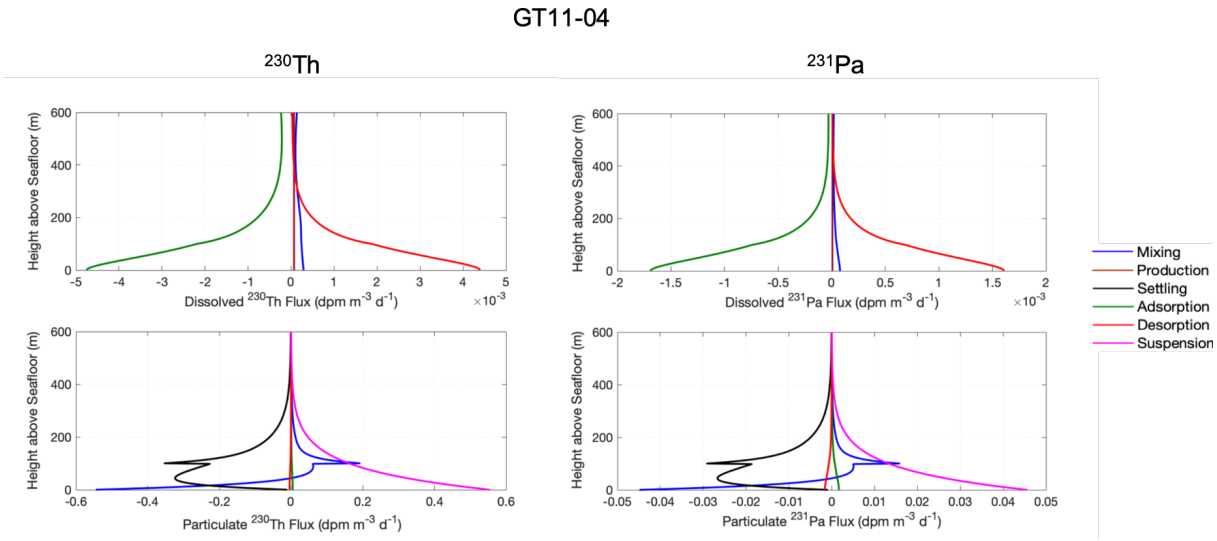

Figure 11: Profiles of radionuclide fluxes in the BNL at station GT11-04 from data inversion. Discontinuities in the fluxes near the interface between the BML and the upper BNL ($z = 100$ m) are due to the different eddy diffusivities across the interface.

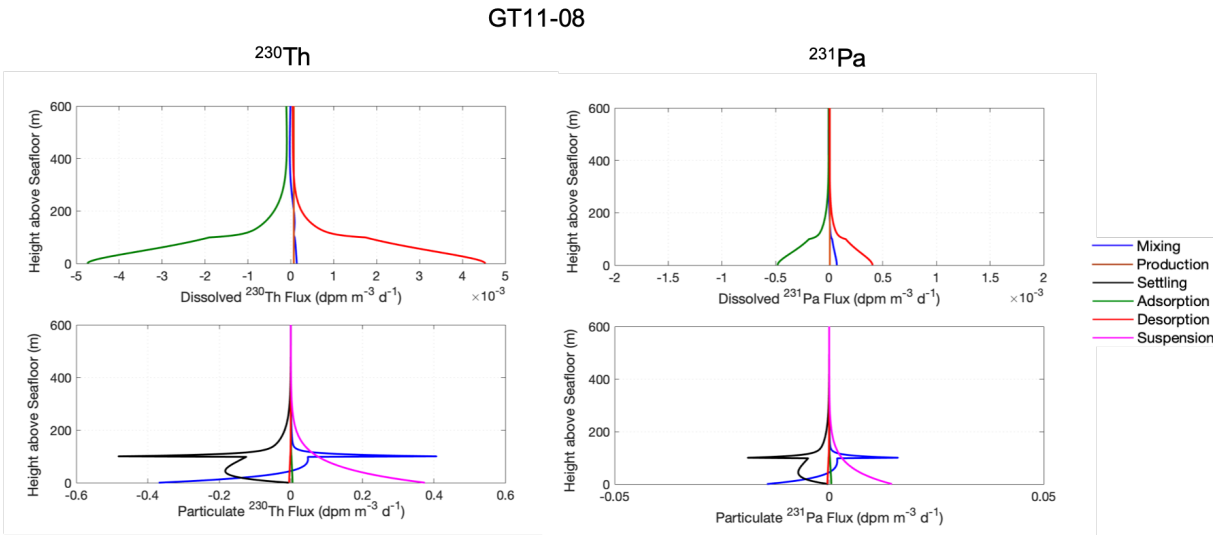

Figure 12: Profiles of radionuclide fluxes in the BNL at station GT11-08 from data inversion. Discontinuities in the fluxes near the interface between the BML and the upper BNL ($z = 100$ m) are due to the different eddy diffusivities across the interface.

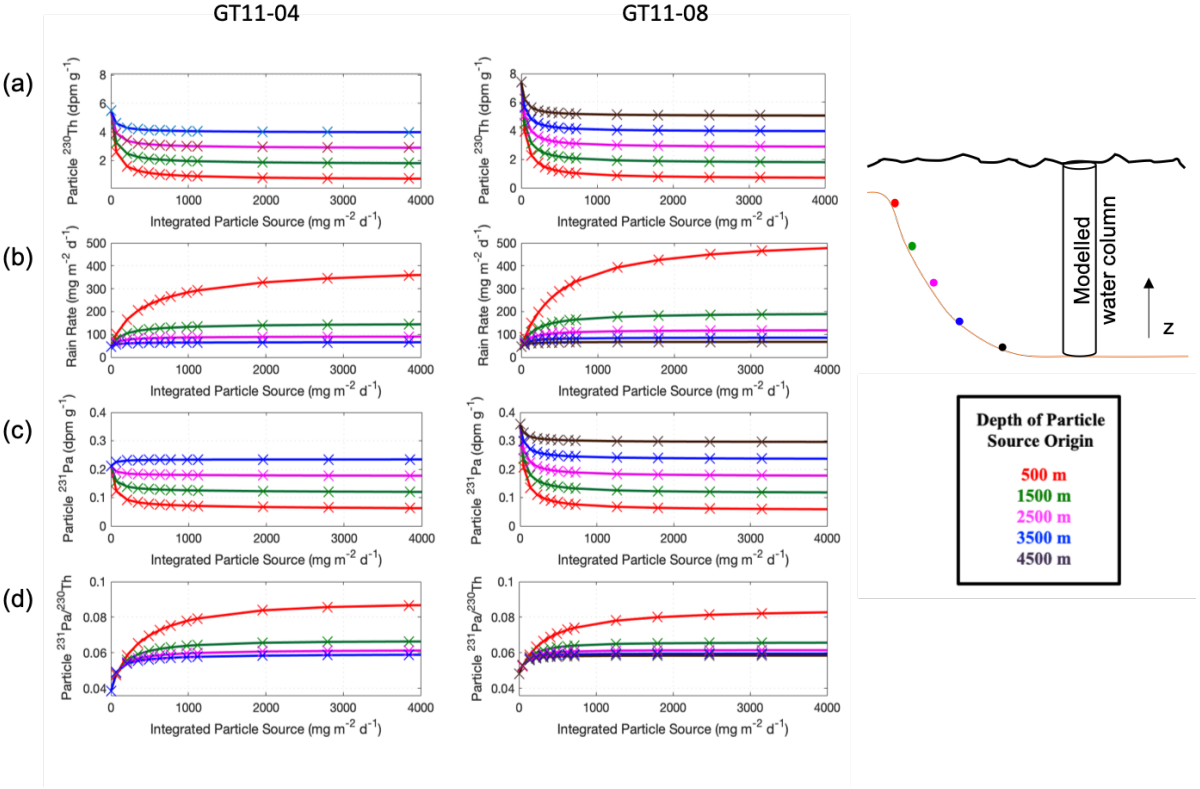

Figure 13: Variations of (a) specific ^{230}Th activity of settling particles, (b) ^{230}Th-corrected particle rain rate, (c) specific ^{231}Pa activity of settling particles, and (d) ^{231}Pa/^{230}Th of settling particles with the integrated particle source ($\langle j_c \rangle$) for different particle source depths and thus different source activities. Solid lines show results obtained when $\langle j_c \rangle$ is varied by varying $j_{c,o}$ with δ_r fixed, whereas crosses show results obtained by varying δ_r with $j_{c,o}$ fixed. Left and right panels show variations calculated from posterior estimates of model parameters at stations GT11-04 (bottom depth 3772 m) and GT11-08 (bottom depth 4926 m), respectively. The inset on the right is a schematic showing different origins of source particles in relation to the water column.

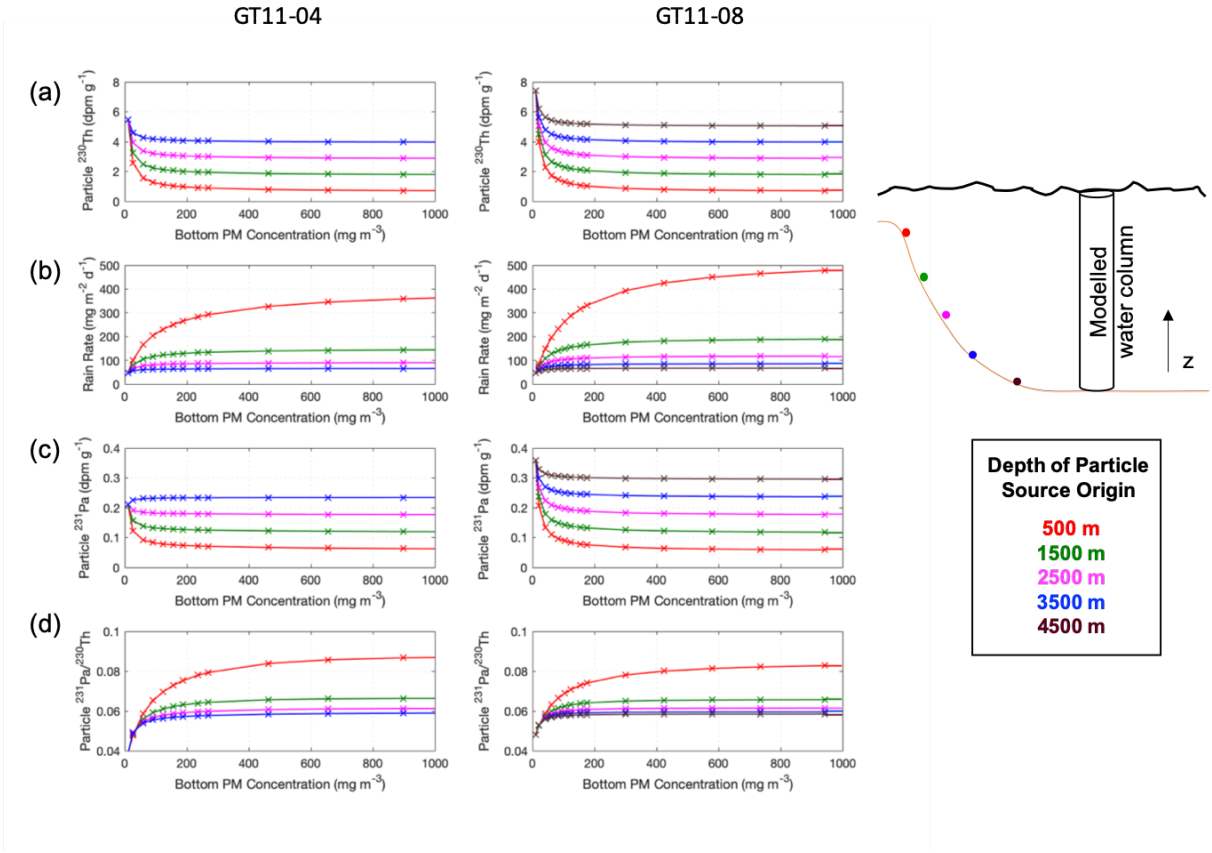

Figure 14: Same as Figure 13, but plotted against mean PM concentration in the bottom 10 m of the water column.

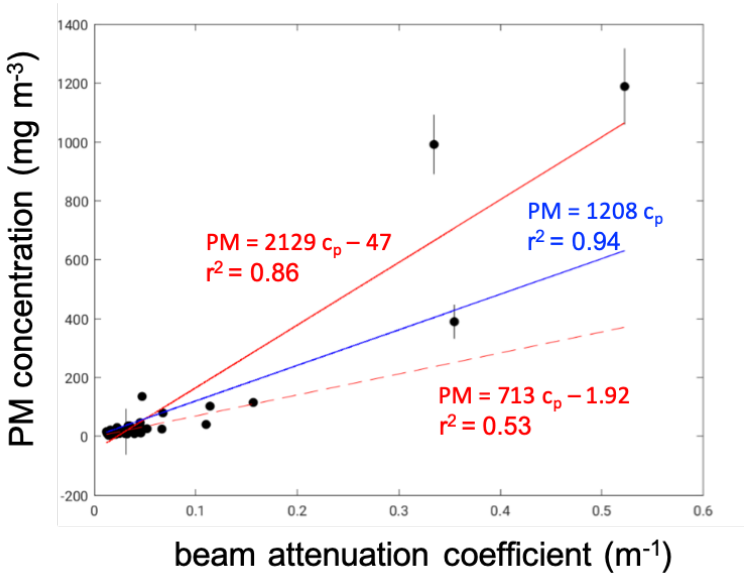

Figure A1: Scatter plot of suspended PM concentration and beam attenuation coefficient (c_p) in deep water along the western margin in the North Atlantic. The black dots are data from GA03 stations GT11-01 to GT11-10 (Lam et al. 2015; Schlitzer et al. 2018). The solid red line is the least-squares fit for these data, and the dashed red line is the least squared fit for these data with the three PM $>$ 200 mg m^{-3} values removed. As a reference, the calibration reported by Gardner et al. (1985b) based on HEBBLE data is also shown (blue).